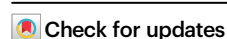# A wireless optogenetic stimulation system for long-term function evaluation of mice forelimb with sub-nerve resolution

Mingjie Zhou[1,6], Biao Yan [1,2,6], Fukui Yang [3,6], Chuxiang Chen[1,6], Fei Wang[1], Chenpei Xu[1], Tingzheng Jiang[4], Kexin Li[1,2], Yuanting Xie[1,2], Hao Zheng[1,2], Chengyang Wang[5], Jiayi Zhang [1,2,7] ✉ & Su Jiang [1,7] ✉

Peripheral nerve transfer is an effective surgical method in restoring motor functions of upper limb after peripheral nerve injuries. However, the outcome of individual function recovery is less predictable. It is crucial to access the long-term evaluation of function improvement. Here, we developed a fully implantable multisite optogenetic stimulation system, which is tailored for wireless, reprogrammable and long-term function evaluation of peripheral nerve plexus with sub nerve resolution. In Thy1-ChR2-EYFP mice, our system induced distinct compound muscle action potentials and forelimb movements when illuminating different nerve fascicles. Furthermore, we applied the system on a nerve transfer mice model after traumatic brain injury and discovered innervation pattern of the transferred and adjacent nerves to multiple muscles consecutively within 12 weeks after surgery. Our system enabled refined evaluation of electrophysiological and motor functions of peripheral nerve plexus, shining light upon personalized diagnosis and treatment after nerve injuries or surgeries.

Peripheral or central nervous system injuries often result in severe sensorimotor deficits in extremities, which significantly impacts patients' quality of life and has become a global burden[1–3]. Peripheral nerve transfer has proved to be an effective approach and utilized in clinical practice to restore motor function[4–6] after peripheral nerve injuries for decades. Recent innovations have expanded its application to central nervous system injuries. In 2018, our team proposed the contralateral cervical seventh nerves transfer (CC7 surgery)[7] technique for treating spastic arm paralysis after cerebral hemisphere injury by surgically establishing ipsilateral connections between the brain and affected upper limb. The results showed significant improvement compared to the currently used rehabilitation interventions[8,9]. Furthermore, the combination of multiple nerve transfer procedures has been proven to effectively improve upper limb function in patients with spinal cord injuries[10]. However, the underlying mechanisms remain poorly understood. To dissect the spatiotemporal changes of nerve and muscle function after peripheral nerve transfer, we necessitate a long-term stimulation platform with sub-nerve resolution to realize the longitudinal tracking of axonal regeneration, functional compensation of adjected nerves,

[1]Department of Hand Surgery, Huashan Hospital, National Health Commission Key Laboratory of Limbs Reconstruction, Shanghai Key Laboratory of Peripheral Nerve and Microsurgery, National Clinical Research Center for Aging and Medicine, Institute of Hand Surgery, State Key Laboratory of Brain Function and Disorders, MOE Frontiers Center for Brain Science, Institutes of Brain Science, Department of Hand and Upper Extremity Surgery, Jing'an District Central Hospital, Fudan University, Shanghai, PR China. [2]Institute for Medical and Engineering Innovation, Department of Ophthalmology, Eye & ENT Hospital, Fudan University, Shanghai, PR China. [3]Sainsbury Wellcome Center, University College London, London, UK. [4]Department of Hand Surgery, Department of General Medicine, Huashan Hospital, Fudan University, Shanghai, PR China. [5]MicroPort Neuronical MedTech (Shanghai) Co. Ltd., Shanghai, PR China. [6]These authors contributed equally: Mingjie Zhou, Biao Yan, Fukui Yang, Chuxiang Chen. [7]These authors jointly supervised this work: Jiayi Zhang, Su Jiang.
✉e-mail: jiayizhang@fudan.edu.cn; oscarjiangsu@126.com

and improvement of limb muscle function during the post-surgery recovery.

The peripheral nerves, especially at high levels, consist of bundles of nerve fascicles that intricately innervate various muscle groups[11,12]. This anatomical characteristic requires a neuromodulation technique capable of selectively targeting distinct nerve fascicles, as thin as 250 µm in diameter, from different angles to achieve sub-nerve resolution in small animal models[13]. Over the past decades, optogenetics has been widely used in central nervous system modulation[14–16] due to its higher spatiotemporal precision compared to electrical modulation, which is ideal for achieving sub-nerve resolution in the peripheral nerve. Some pioneering studies have explored the potential for vision restoration in blind patients[17,18], showing the great clinical translational potential of optogenetics technology.

However, there have been limited reports on optogenetic devices capable of long-term reliable performance in small animals. Our team previously reported that C7 nerve regeneration and brain reorganization in mice after crossing nerve transfer require about 12 weeks[19], and the time course of the rehabilitation would be even longer in humans due to the slow rate and long distance of axonal regeneration[20,21]. This imposes higher requirements for the longevity of the device.

Hence, in this study, we developed a fully implantable multisite optogenetic stimulation system (FIMOSS) that provided both sub-nerve resolution and device longevity, which we utilized to track peripheral nerves' functional reorganization after nerve transfer surgery. This new technology proceeded from our previously reported multisite optogenetic stimulation device (MOSD), which provided a machine-nerve interface for acute activation of different nerve fascicles in the C7 nerve, effectively inducing various movements of forelimbs in mice[22,23]. In FIMOSS, we advanced this method for chronic use by integrating wireless technology into an optogenetic implant that can fit comfortably on a mouse's chest. The implant consists of a cuff optrode with a similar structure as MOSD (we called it MOSD II), which can be wirelessly powered and controlled to execute various stimulation parameters after implantation in mice and maintained stable performance for at least 12 weeks. To further validate this method, we successfully induced distinct forelimb movements via sub-nerve optogenetic stimulation on brachial plexus in Thy1-ChR2-EYFP mice and elaborated the change pattern of brachial plexus function reorganization in a nerve transfer mice model after traumatic brain injury (TBI) and CC7 surgery. These findings suggest that the system can serve as an effective experimental tool for long-term electrophysiological and induced-behavioral studies on peripheral nerve plexuses function after injuries or nerve surgeries in mice or other larger animal models. Additionally, it offers the potential for multisite stimulation with sub-nerve resolution and various limb movement control.

Results

Design and characterization of FIMOSS

The FIMOSS consisted of an implant (Fig. 1a) and an external device. The MOSD II of FIMOSS implant can flexibly encircle the peripheral nerve, and different µLEDs can activate distinct nerve fascicles from different angles with sub-nerve resolution (Fig. 1b). The FIMOSS implant was designed to be fully implantable for long-term in vivo stability, miniaturized and battery-free to fit comfortably in mice (Fig. 1c), while providing programmable wireless multisite optogenetic stimulations to brachial plexus nerve trunk fascicles (Fig. 1d, e) with four channels of spatial resolution. The system was designed to wirelessly power the implant at the resonant frequency of 2 MHz, and also to wirelessly transmit stimulation command from a PC to the implant. Users can interface with the PC to update the stimulation parameters of the device, even after it has been fully implanted. The total weight of FIMOSS implant was 0.127 ± 0.005 g ($n = 6$), which occupied around 0.5% of an average mouse body weight across the experiment duration

(average was 25 g) to maximally preserve naturalistic behavior in mice[24,25]. The FIMOSS implant was also designed for manufacturability, which leverages commercially proficient Printed Circuit Board and Assembly (PCBA) production lines for complete fabrication and assembly. This minimizes specialized manual assembly of the µm-scale electronics, enabling consistent mass production at a low cost.

Electronic design of FIMOSS

The overall shape of the FIMOSS implant is similar to that of a cochlear implant, but is much smaller in size (Fig. 2a). The geometry of the FIMOSS implant consisted of a driver region that was a 4.5 mm by 4.0 mm square closely connected with a circle of 5.0 mm in diameter (Fig. 2b). The interconnect extended from the driver with a length of 0.64 mm, which was design to reach the brachial plexus in depth through a pectoralis major incision from the subcutaneous ipsilateral chest wall (Fig. 2c). The antenna region was in plane with the rest of the driver FPC, rather than being stacked on top of it to optimize for device thickness due to fragility of the skin, and subcutaneous space was still sufficient to fit the device (Fig. 2c). The circuit board thickness of the driver region was 0.29 mm (1.2 mm with components), and the total device thickness increased to 2.2 mm after encapsulation, as 500 µm of encapsulation was added to each side. The interconnect and the nerve cuff extended from the driver were 0.065 mm thick, and increased to 0.365 mm after PDMS encapsulation (Supplementary Fig. 1a, b).

The electronic hardware of the driver region was a 6-layer flexible printed circuit (FPC) Board containing the printed antenna, and the driver circuitry mounted with a micro-controller-unit (MCU), supporting electrical components, and backup solder pads to provide compatible extensions for MOSD[22] reported by Zheng et al. previously (Supplementary Fig. 2). The positioning eyelet in the center of the antenna served as a hanging point during the Parylene C coating process, and further assisted device positioning during the PDMS encapsulation process. One layer (Layer4, Supplementary Fig. 1b) of the FPC extended outward and served as the flexible interconnect and the MOSD II (a modified version of MOSD) with four on-board µLEDs that interfaced with the target nerve.

In order for the implant to be manufactured in whole from commercial PCBA production companies with a low cost, the PCB layout design complied with a minimum trace width/clearance of 2.5/2.5 mil, and only used 0.10/0.30 mm through-hole for vias. For component selection, a type of µLED chip with flip chip packaging was selected to replace the commonly used CREE µLED chips that have wire bond packaging[26], as we were able to find standardized manufacturers that were proficient with assembling the flip chip µLED to the FPC board (Fig. 2d). This µLED emits light at a dominant wavelength of 465 nm that was compliant with the activation criteria of ChR2 in our subjects. More importantly, the flip chip µLEDs have a pair of solder pads that were bigger in surface area and were more spatially separated from each other than the wire bond µLED chips. These two features of the bonding pads enabled the flip chip to form a stronger bond with the FPC mounting pads, hence reducing the chances of failure due to fracture of µLED solder joints. This manufacture-in-whole design was one of the biggest improvements from the previous design that benefited both long-term reliability and manufacturability of the FIMOSS implant.

Mechanical characteristics and encapsulation of FIMOSS

For encapsulation of the FIMOSS implant, the driver region was coated with a thin layer (12 µm thick) of Parylene C, and was further encapsulated with PDMS to provide a mechanically soft and biocompatible exterior to interface with the implantation site (Fig. 2d). Parylene C was selected due to its excellent biocompatibility and low permissibility of water[27,28]. Aside from the driver region, the interconnect and the MOSD II regions were coated with a layer (~150 µm thick) of PDMS to protect
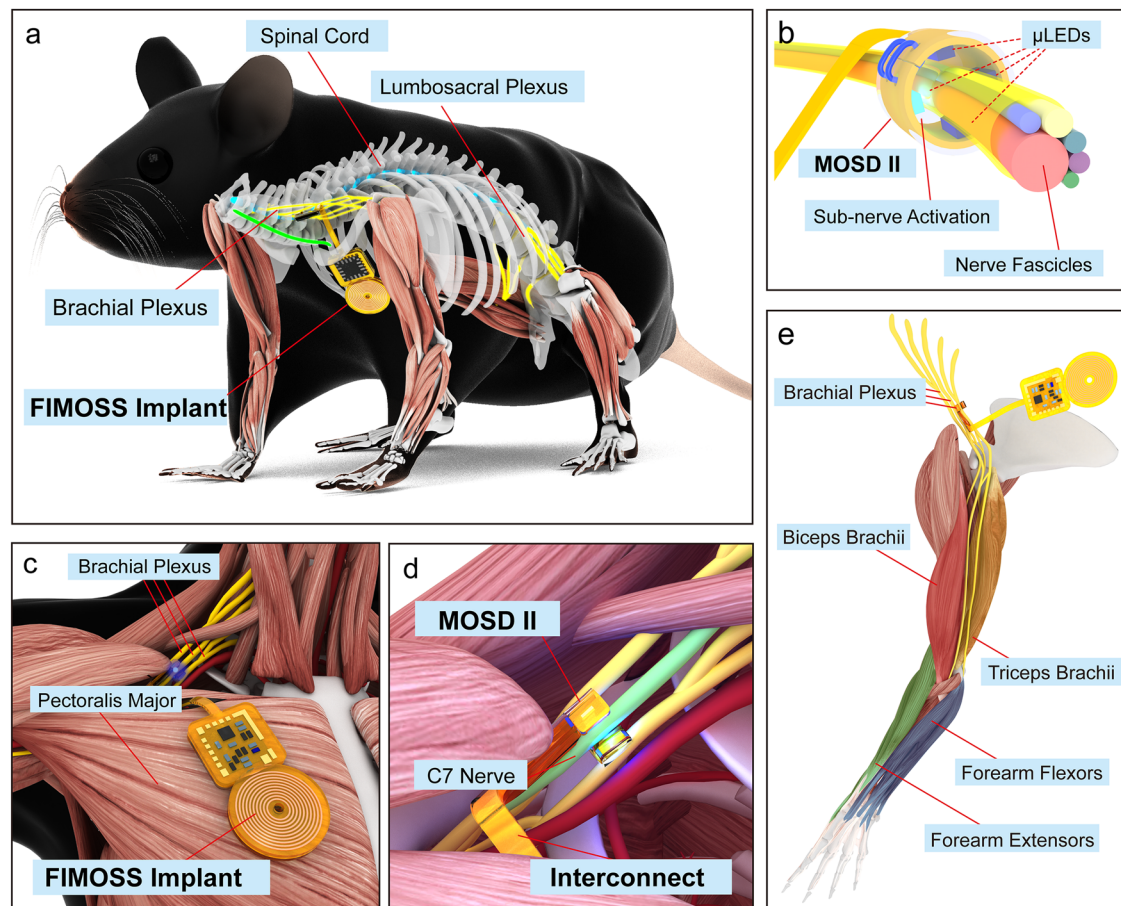
Fig. 1 | Schematic of FIMOSS for long-term function evaluation of peripheral nerve plexus. a The FIMOSS implant, which was comprised of multiple μLEDs to realize multisite neuromodulation, was designed for optogenetic stimulation of peripheral plexus in mice, such as brachial plexus. **b** Diagram of the layout of the cuff optrode (MOSD II) surrounding along the length of peripheral nerve. A μLED activates a single nerve fascicle with sub-activation resolution. **c** When applied on the brachial plexus, the main body of the FIMOSS implant was fixed on the surface of the pectoralis major, while MOSD II and the interconnect interfaced with the brachial plexus through an incision of the pectoralis major. **d** MOSD II has 4 μLEDs on the flexible substrate, which can wrap around the nerve trunk of the brachial plexus (middle trunk as an example) and stimulate the nerve with sub-nerve resolution. **e** Distinct forelimb muscle groups activated by different μLEDs of FIMOSS implants. Contraction of muscles, including biceps brachii, triceps brachii, forearm extensors and flexors can be induced, respectively. Biceps brachii, red. Triceps brachii, yellow. Forearm extensors, green. Forearm flexors, blue.

the electronics while preserving the mechanical flexibility of the FPC. This PDMS layer also provides a cushion between the nerve and the electronics, as the mechanical property, namely the Young's modulus of PDMS was similar to that of the target nerve[26]. Even though PDMS has a higher water permissibility than Parylene C[29], since the electronics that it protects was much simpler and more robust than the driver, the current PDMS coating was sufficient to maintain functionality of MOSD II for 3 months of in vivo operation in all mice reported in this work, which was predicted prior to implantation by accelerated aging in 60 °C saline (Supplementary Fig. 3 and Supplementary Movie 1).

The mechanical design for the MOSD II, which consists of the interconnect and the μLED cuff, was a major challenge. The current form resulted from rapid prototyping and surgical testing of potential designs according to the anatomical characteristics of the brachial plexus in mice. Due to the anatomic complexity, the interconnect took the form of a straight line, rather than employing some of the previously reported designs, such as the serpentine-shaped interconnects[26]. Although the serpentine shape had superior mechanical flexibility, four channels worth of electrical traces can only fit in the narrow surgical route in our case if packed closely in a linear shape. Once the interconnect reached the brachial plexus, its shape then took an L-turn towards the center (longitudinal axis) of the subject's body so that the short arm of the "L" aligns with the direction of brachial plexus nerves (Fig. 2e). This was to

minimize chances of shear cut to the nerve by the FPC during the animal's arm movement. At the end of the interconnect, the flexible FPC carrying 4 μLEDs was designed to be curled and sutured into a cuff to interfaced with the target nerve.

The FPC thickness of MOSD II was 65 μm, and this thickness was validated to be flexible enough for the interconnect to reach brachial plexus, and for the cuff to form around the nerve and held together by 11–0 prolene suture through the suture eyelets (Fig. 2e). The width of MOSD II was 0.79 mm, and it was within the maximum exposure window of the nerve through the subclavian incision (1–1.5 mm). The size of the μLED was 152 μm by 406 μm, and 100 μm thick. The spacing between two neighboring μLEDs was carefully designed to be 400 μm. This value was reverse calculated to enable MOSD II to fit on the range of nerve diameters from 250 mm to 600 mm, and the 4 μLEDs were equally distribute over the cuff circumference for the typical nerve diameter of 380 μm (Fig. 2f–h).

Four suture eyelets were positioned on each side to enable MOSD II to be adjusted for a secure and adaptable fit around varying diameters of nerves. The two exterior eyelets on each side can also be sacrificial for the pre-curling process of the cuff (Supplementary Fig. 4). The diameter of the eyelets was 0.1 mm to both consider for manufacturability using the more accessible drilling technique, and to allow for 11–0 prolene suture to pass through.
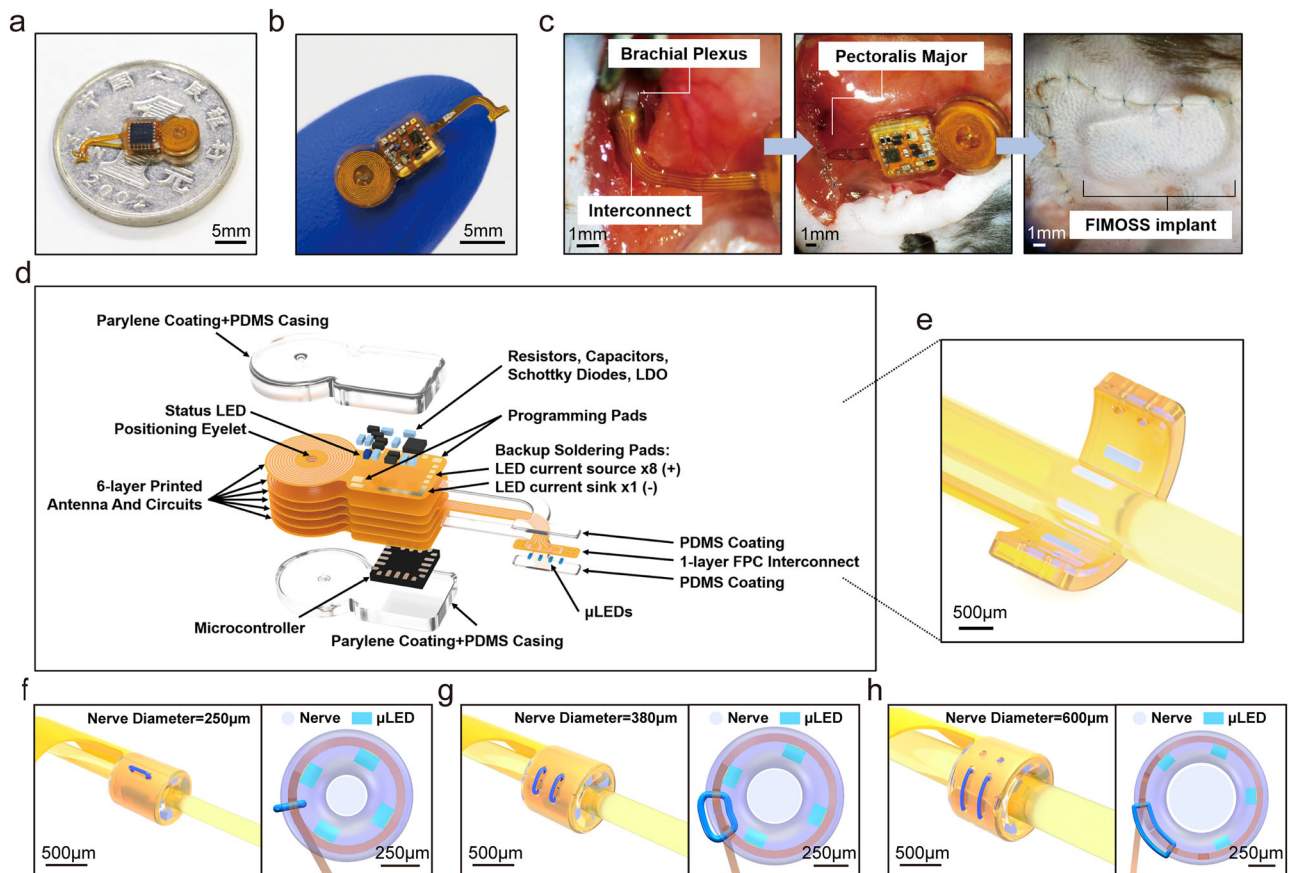
Fig. 2 | Design and structure of FIMOSS implant for long-term multisite optogenetic stimulation. a, b Photographs of a FIMOSS implant that consists of a cuff optrode (MOSD II), interconnect, driver and antenna (scale bar = 5 mm); image of the front side of a FIMOSS implant placed near a coin (**a**), image of the reverse side of a FIMOSS implant (**b**). **c** Intraoperative photographs of a FIMOSS implant during the implantation surgery. (scale bar = 1 mm) Three parts of the FIMOSS implant were fixed at the designed positions: (i) MOSD II wrapped around the brachial plexus (C7 nerve as an example), (ii) the interconnect through an incision on the pectoralis major, (iii) the driver and antenna on the surface of the ipsilateral pectoral major. **d** A layered schematic illustration of FIMOSS implant. **e** The interface between the nerve and MOSD II. (scale bar = 500 μm) **f**–**h** Different stitching and fixation method (left, scale bar = 500 μm) and cross-section diagram (right, scale bar = 250 μm) of MOSD II adapted to nerves of different diameters. **f** The outer and inner suture eyelets were sacrificed and overlapped respectively to wrap around the nerve with a diameter of around 250 μm. **g** The outer suture eyelets were sacrificed while the inner eyelets were sutured to adapt to a nerve with diameter of 380 μm. **h** The outer suture eyelets were sutured to adapt to a nerve with a diameter of 600 μm.

Wireless characteristics of FIMOSS

Wireless powering of the FIMOSS implant was achieved by resonant inductive coupling at 2 MHz between the transmitting antenna on the external device and the receiving antenna on the implant (Fig. 3a and Supplementary Fig. 5a). The receiving antenna (or coil) on the implant was composed of printed copper traces with 10 turns on each layer connected across the 6 layers. The diameter of the most outer turn was 5 mm, and the trace width and clearance used for this antenna was 3 mil/3 mil. The copper thickness for the trace was 1/3 ounces. The inductance of this coil design was predicted to be 9.98 μH by TI Coil Designer, and measured to be 10.0 μH at 2 MHz.

The receiving antenna was matched with a pair of capacitors (610 pF in total) in parallel to form an inductor capacitor resonator (LC resonator) with a resonance frequency of 2.04 MHz. The transmitting antenna was programmed to emit radio frequency (RF) at 2 MHz, matching the receiver's resonance frequency; thus, the implant was able to efficiently receive power from the emitting antenna through resonant inductive coupling. The printed antenna had a decisive advantage over a copper-wire antenna in manufacturability and consistency, as it eliminated the manual steps to assemble the antenna. The printed antenna had a quality factor (Q) of 14.8. Thermal stability experiments were also conducted on the printed antenna, and it showed that this antenna was thermally safe for implantation under typical operating condition (Fig. 3e–g).

One-way wireless communication was achieved on FIMOSS to send stimulation parameter updates from the external device to the implant (Fig. 3a). The external device switched on and off the power emission (amplitude modulation) to encode the message at 1.2 kHz, and the implant received and decoded the message with a rather simple decoding circuit (Fig. 3b). The decoding circuit used two Schottky diodes to serve as a barrier to separate the fluctuating RF signal from the buffered VCC line. The inductor (L1) and capacitor (C3) served as a power bank to buffer the VCC to maintain running of the MCU, while the amplitude modulated RF signal fluctuates sharply for the USART_RX port to detect (Fig. 3c). As a result, USART_RX port of the MCU was able to successfully receive the parameter update messages via its universal asynchronous receiver/transmitter (UART) peripheral at a baud rate of 1200 bits s⁻¹ (Fig. 3c and Supplementary Movie 2).

The wireless power transfer capability of the FIMOSS implant was evaluated by a load sweep sourcing power from the implant while it was wirelessly powered by the external device under the default wireless condition (external device set at 3.3 V, 60–80 mA; the emitting antenna and receiver antenna were concentrically aligned, in parallel, and 1 mm apart). The load sweep showed that the implant was able to maintain the target voltage output of 3 V when the load is sourcing 4 mA or less (Fig. 3d). The current consumption of the implant (when operating at 3 V) was characterized to be between
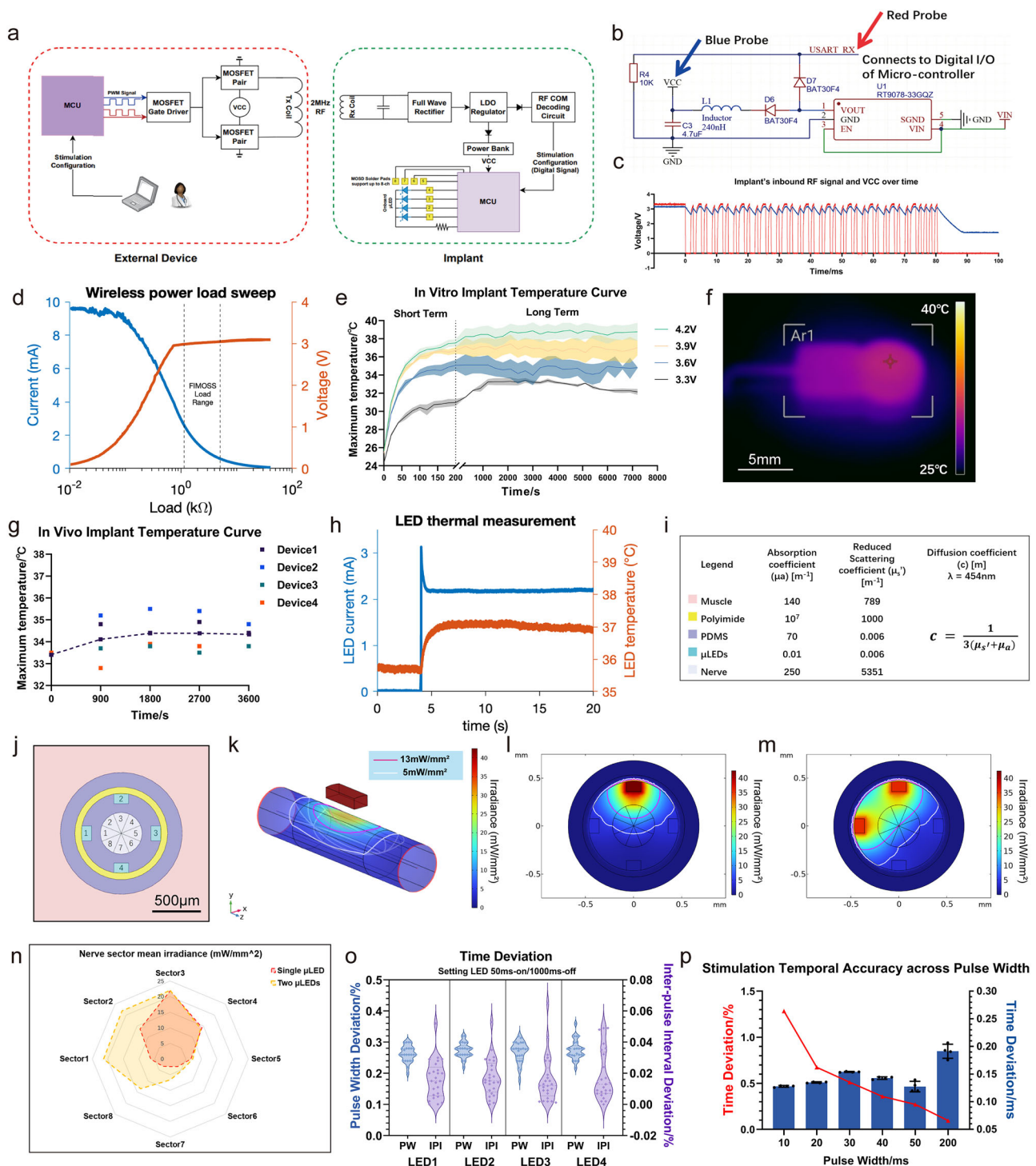
0.6 mA when idle to 2.6 mA when stimulation was on (Supplementary Fig. 6a). Thus, we confirmed that the default wireless condition was sufficient to support the power budget of the implant.

External device and embedded software

The external device consisted of a PCBA embedded system mounted with a DC power connector, two additional connectors for firmware programming and serial interface with a personal computer (PC), a copper wire coil as the transmitting antenna, and a pair of 3D-printed cases to package all the parts neatly for daily uses (Supplementary Fig. 5b, c). The external device was designed to shape as a hand-held mini scanner for the ease of use during implantation procedure for

validating MOSD II has been properly positioned, and other stimulation scenarios after FIMOSS implant has been implanted.

ATMEGA328PB-MU was selected as the MCU of the embedded system to enable relatively easy software development through the Arduino Integrated Development Environment (IDE). The external device currently has two modes of operation (Supplementary Movie 2). Mode 1 was to simply provide wireless power to the FIMOSS implant. And mode 2 was to transmit stimulation commands to the implant while powering the implant. Under mode 1, the external device was powered by a DC power source at 3.3 V, and operates with a typical current of 60–80 mA. In this case, the MCU sends a pair of pulse width modulated (PWM) signals with inverse polarity at 2 MHz and 50% duty

Fig. 3 | Characterization of FIMOSS implant. System diagram (**a**), electrical schematic (**b**), radio frequency communication signal (**c**) of FIMOSS. **d** Current and voltage across a variable load resistor while it sourced power from the FIMOSS implant that was wirelessly powered under the default wireless condition. The two vertical lines corresponds to the minimum (0.6 mA) and maximum (2.6 mA) current consumption of the FIMOSS implant at 3 V. **e** The temperature changes in vitro during the 7200 s' continuous working with four different input voltages. ($n = 4$, 20 ms pulse width, 1000 ms inter-pulse interval, mean ± s.e.m.) FIMOSS implants were placed on a 1mm-thick glass slide, and the external device antennas were fixed underneath the slide. Voltages of the DC power supply were adjusted to 3.3 V, 3.6 V, 3.9 V, and 4.2 V to power the external device, which wirelessly drive the FIMOSS implants. **f** A representative infrared thermographic image of FIMOSS when working in vitro. (Input voltage = 3.3 V, 20 ms pulse width, 1000 ms inter-pulse interval, scale bar = 5 mm) **g** The temperature changes of FIMOSS implants in vivo during the 3600 s continuous working. ($n = 4$, input voltage = 3.3 V, 20 ms pulse width, 1000 ms inter-pulse interval) FIMOSS implants were implanted subcutaneously on the surface of pectoralis major, whose temperature were measured by an infrared thermometers **h** Temperature change of the μLED in vivo during a 20 s test period, where the current through the μLED was simultaneously recorded. The μLED was powered by a constant current source that was set to 2.1 mA. **i** The absorption coefficients and reduced scattering coefficients used for the optical simulation. **j** Cross-sectional view of the 3D model of a MOSD II cuffing on a typical

target nerve (440 μm diameter, scale bar = 500 μm). This 3D model was used in the optical simulation, and each domain was color-coded corresponding to the color legend in (**i**). The 4 μLEDs were numbered, and the nerve was equally divided to eight sectors and numbered as references for the quantitative analysis result in (**n**). **k** Heat map of the light irradiance distribution in 3D optical simulation, when 1 μLED was illuminated at 2.5 mW of optical power. The color legend is the same as in Fig. 3i, m. Domains except for the activated μLED and the target were hidden. The plot was set at 40% transparency to allow visualization of the contour lines of 13 mW mm^{-2} and 5 mW mm^{-2} depicted in magenta and white. **l, m** Heat map of light irradiance in a representative 2D slice out of the 3D optical simulation result. The 2D slice was defined as the *XY*-plane slicing down the middle (*Z*-direction) of the μLED in (**k**). One μLED (**l**) was illuminated at the standard optical power of 2.5 mW. Two neighboring μLEDs (**m**) were illuminated at a reduced optical power of 2.0 mW. The color bar represents light irradiance in mW mm^{-2}. **n** The average irradiance in each sector of the nerve computed by optical simulation of 1-μLED (orange) and 2-μLED (yellow) illumination in Fig. 3l, m. **o** Time deviation (**o**) of 4 μLEDs' light (blue, left *y* axis) and interval time (purple, right *y* axis) when the stimulus parameter was set to 50 ms pulse width, 1000 ms inter-pulse interval. **p** The correlation of pulse width and time accuracy when the pulse width was set to 10, 20, 30, 40, 50, and 200 ms. Relative (red, left *y* axis) and realistic time deviation (blue, right *y* axis) of μLEDs were recorded or calculated, respectively ($n = 4$, mean ± s.e.m.).

cycle to drive the metal-oxide-semiconductor field-effect transistor (MOSFET) gates (Fig. 3a). The two pairs of MOSFET gates, each driven by one of the PWM signal, connected one end of the coil to high voltage and the other end to ground in one instance, and reversed to connecting one end to ground and the other end to high voltage in the next instance. This switching happened at the frequency of the PWM signal (2 MHz), and generating a back and forth current across the coil at 2 MHz, and hence creating an oscillating magnetic field that emitted the 2 MHz RF wave to power the implant via its receiving antenna.

Under mode 2, in addition to the condition in mode 1, the external device was also connected to a PC via a USB-to-UART serial adapter. The user interfaces with the PC software to input the stimulation command on PC. The PC software sends the command to the external device via the serial adapter using UART protocol. The external device received the message and relayed the message's binary data to gate the on and off of the PWM outputs that powered the coil. This technique encodes the message in amplitude modulated RF signal with UART protocol's timing diagram to wirelessly send the data to the implant at a baud rate of 1.2 kHz.

In the FIMOSS implant, the on-board MCU carries the embedded software (Supplementary Fig. 7) that executes the stimulation strategy designed by user, and manages the wireless communication from the external device. The decoded communication signal was wired to the USART_RX pin of the MCU. The MCU sampled the signal, and upon reception of the correct binary keys and successful parity check, it translates the received packet into a stimulation strategy using a pre-programmed look-up table (Supplementary Tables 1, 2, and 3). The translated stimulation strategy was then written into the non-volatile memory (electrically erasable programmable read-only memory, EEPROM) of the MCU. As the MCU was programmed to read from its EEPROM every boot up to run the stored stimulation strategy, it has now been reprogrammed to run the new strategy.

This communication scheme enabled flexible updates of any of the three stimulation parameters: LED_ID (range 1–8), pulse width (range 0–150 ms, and special case of 200 ms), and inter-pulse interval (range 0–3 s, and special case 30 s).

Accelerated aging test of FIMOSS in vitro

To evaluate the long-term reliability of FIMOSS implants, we conducted an accelerated aging test in vitro to simulate 12 weeks of in vivo operation. 10 eligible FIMOSS implants were immersed in saline solution at 60 °C, and their performance was tested and recorded daily. The results showed that all 10 implants maintained normal operation

for the 19-day test period. All the μLEDs and status LEDs illuminated normally, and the reprogramming capability of all the FIMOSS implants was preserved (Supplementary Movie 1). According to the acceleration aging formula, water bath in saline solution at 60 °C will accelerate device aging by a factor of $2^{2.3} \approx 4.92$. Then, surviving 19 days in the accelerated aging condition was equivalent to surviving at least 93 days (≈13 weeks) in vivo. This result confirmed that the encapsulation can effectively waterproof the implant for chronic use. Hence, the FIMOSS implants were predicted to be capable of delivering continuous operation for 12 weeks in vivo, which was required by our animal experiments.

Thermal and optical characteristics of FIMOSS implant

Sufficient optical power is essential for effective peripheral nerve stimulation. However, excessive optical power can lead to heating of FIMOSS implants, which may injury the skin or interpret the normal function of nerves.

Therefore, temperature change of both the driver and the μLED were measured to evaluate the thermal safety of the FIMOSS implant. On the FIMOSS implants, we first tested the thermal impact of different levels of external device's input power. When the external device was set to an input voltage of 3.3 V (typical operating current 60–80 mA), which was the lowest input voltage that can drive the implants, the temperature of FIMOSS implants rose from 25 °C (room temperature) and stabilized at 32 °C in vitro (Fig. 3e). The most significant temperature increase occurred on the receiving antenna (Fig. 3f). When tested in vivo, temperature rise of the implants never exceeded 1 °C during a 3600 s testing period (Fig. 3g). When the input voltage of the external device gradually increased from 3.3 V to 4.2 V, the temperature rise of the implants also increased significantly (Fig. 3e). As the external device operating at 3.3 V can already support the power budget of the implant, for the in vivo experiments in mice, we opted to use 3.3 V as the default operating voltage for the external device, as it was demonstrated to be thermally safe.

The temperature change within the μLED nerve cuff was also measured in vivo by replacing the nerve with a thermistor of the same size. Under the extreme case of constant illumination at 2.1 mA, the μLED temperature increased from 36 °C (body temperature) and stabilized to 37 °C during the 20 s testing period (Fig. 3h). The realistic operating condition of the μLEDs used in our animal experiments was far less demanding, where the μLED was activated using 2.0 mA of current (Supplementary Fig. 6a), and with a low duty cycle (~1%) in the typical stimulation parameter of 20 ms pulse width and 2000 ms inter-
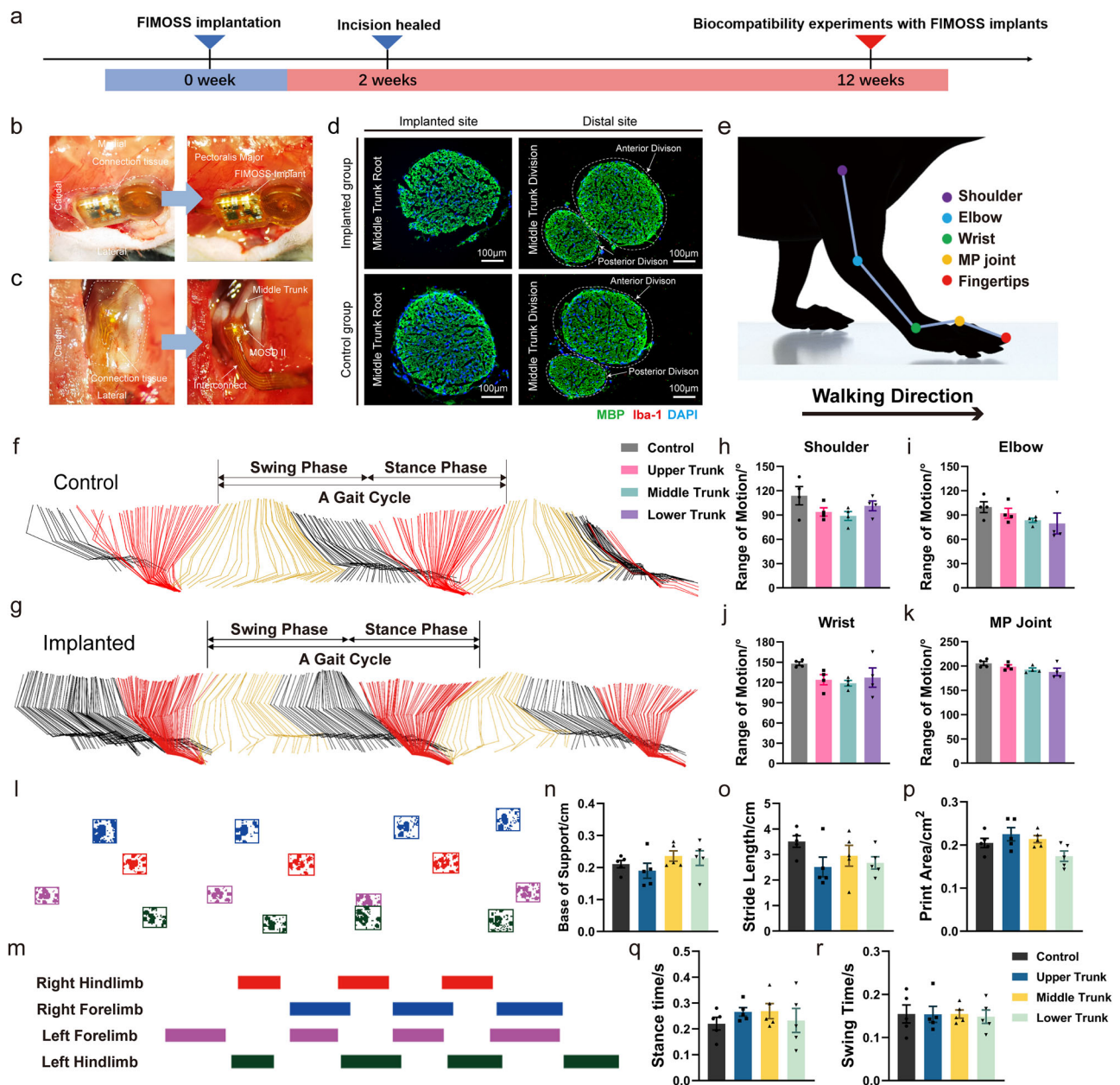
Fig. 4 | Biocompatibility of long-term FIMOSS implantation in brachial plexus after 12 weeks. a Timeline of FIMOSS implantation and biocompatibility experiments. **b** Intraoperative images of the FIMOSS implant 12 weeks after implantation surgery. The PDMS encapsulation was observed to be intact after removing the thin layer of connective tissue encapsulation. **c** Intraoperative images of MOSD II and brachial plexus 12 weeks after implantation surgery. The texture and continuity of middle trunks and adjected upper and lower trunks were not affected by the implantation of MOSD II. **d** Immunofluorescent image of middle trunks at the implantation (main trunk) and distal site (nerve branches) of MOSD II. No obvious inflammation response can be observed. (scale bar = 100 μm) (n = 6). **e** A Schematic of motion analysis experiment set-up. **f, g** Representative trajectories of forelimb movements in mice from control group without FIMOSS implant (**f**) and middle trunk implantation group with an FIMOSS implant 12 weeks after implantation (**g**). Several gait cycles were showed in the image. Golden and black lines represented the forelimb trajectory of lifting and landing process (swing phase). Red lines represent the stance phase. Comparison between range of motions of shoulder (**h**), elbow (**i**), wrist (**j**), and MP joint (**k**) in different groups in motion analysis experiments. **l, m** A Representative photograph of walking tracks captured by the gait analysis system. Quantification analysis shows base of support (**n**), stride length (**o**), print area (**p**), stance time (**q**), and swing time (**r**) of right forelimb were not significantly affected when a FIMOSS implant was implanted onto the upper, middle, lower trunks on the right side. n = 4 for each group in motion analysis (**h**–**k**). n = 5 for each group in gait analysis (**n**–**r**). One-way ANOVA and multiple comparison tests with Dunnett's correct. Data are presented as mean ± s.e.m.

pulse interval. Hence, both the μLED and the driver were deemed to be thermally safe for animal experiments, and further confirmed by intraoperative observation and immunofluorescence staining of the nerves and tissues near the implantation site that showed no signs of heat damage (Fig. 4b, c).

Light-current-voltage sweeps were conducted to characterize the μLED's optical power output as its current increased from 0 to 10 mA. FIMOSS implant used an 160 Ω current-limiting resistor in series with

the μLEDs, which limited the current through μLED to 2.0 mA resulting in an optical power output of 2.5 mW (Supplementary Fig. 6b).

A set of 3D finite element analysis (FEA) studies were performed to simulate the propagation of light irradiance from the μLED (2.5 mW optical power, 42 mW mm^{-2} irradiance at μLED's surface) in the implanted environment (Fig. 3i–k). A 2D representative slice out of the 3D result was used to visualized the irradiance distribution in the cross-section of the nerve fiber, where contour lines of 13 mW mm^{-2} and

5 mW mm^{-2} irradiance were illustrated (Fig. 3l, m). These two irradiance thresholds were chosen because the transgenic mice line Thy1-ChR2-EYFP has been previous characterized that the muscle force elicited by optogenetic stimulation of the peripheral nerve reaches 50% of the maximum force when light irradiance is 5 mW mm^{-2}, and reaches the maximum force at 13 mW mm^{-2} or higher[30].

When one μLED (μLED2 in this simulation) was activated at the standard optical power of 2.5 mW, sector 3 that directly faced it received an average irradiance of 21.9 mW mm^{-2}, where sector 7 that was further away from it only received an average irradiance of 2.5 mW mm^{-2} (Fig. 3l, n). Despite the two sectors are only ~300 μm (centroid-to-centroid distance) apart, a fascicle in sector 7 would elicit 90% less force than a fascicle in sector 3 due to the irradiance differences[30]. Therefore, we estimate the spatial resolution of FIMOSS's optogenetic stimulation to be around 300 μm. This demonstrated irradiance gradient was expected to allow for selective activation of a sub-section of the target nerve. By illuminating different μLEDs, fascicles across different sections of the nerve can be targeted, thus triggering distinct downstream muscle movements.

To further investigate the effect of optical power on spatial resolution, we conducted additional optical simulation when one μLED was illuminated at the optical power of 2.5 mW, 4.5 mW, and 6.5 mW (Supplementary Fig. 8a–c). Previous studies showed that the spike probability of ChR2-expressing neurons ramps up exponentially from 0 to 1 when the received blue irradiance increased from 1 mW mm^{-2} to 10 mW mm^{-2}[31]. The percentage of nerve area that received irradiance above the 10 mW mm^{-2} threshold increased from 33.75% to 61.66% and to 77.45% under these three optical power conditions (Supplementary Fig. 8d). This demonstrated that increasing optical power from the current setting of 2.5 mW would lead to more fascicles within the nerve being activated, thus more unspecific stimulation.

Performing nerve stimulation using only one μLED at a time can create blind spot at the corner sectors (sector 2,4,6,8 in Fig. 3j), because there were no μLEDs directly facing them. Therefore, further FEA study was done when two neighboring μLEDs were simultaneously illuminated in a reduced optical power of 2.0 mW each to explore resolution of the blind spot issue. The FEA result showed that in this manner, the corner sectors can receive the same level of mean irradiance as the sectors that have μLEDs facing them (Fig. 3m, n). Hence, this modality of illumination can ensure that all sectors of the nerve are accessible by optogenetic activation.

Temporal characteristics of FIMOSS

In order to meet different experimental needs, such as compound muscle action potentials (CMAP) experiment and achieving precise control over the range of motion of multiple joints in the forelimb in mice, we designed multiple reprogrammable stimulation parameters, including μLED-selection, pulse width, inter-pulse interval for the FIMOSS implant (Supplementary Tables 1, 2, and 3). In this case, it is crucial to validate that the control of the μLED's optical pulse width and inter-pulse interval is temporally accurate; thus, we conducted an experiment measuring μLED optical power during activation to validate FIMOSS implant's time control precision.

A total of 6 different stimulation parameters were tested, including five commonly used parameters (10/20/30/40/50 ms pulse width, 1000 ms inter-pulse interval) and one parameter with longer durations (200 ms pulse width, 2000 ms inter-pulse interval). The 4 μLEDs on MOSD II were activated in sequence, and their time accuracy was evaluated. The results showed that the realistic pulse width of the 4 μLEDs had a deviation of approximately 0.1–0.15 ms and the deviation rate of pulse width was below 0.4% (Fig. 3o), which was not significantly correlated with the setting of μLEDs pulse width (Fig. 3p). For the inter-pulse interval, when set to 1000 ms or 2000 ms, the realistic deviation time was approximately 0.5–1 ms, with a deviation rate of around 0.1% (Fig. 3o). Additionally, during the 2-min detection period,

the time accuracy of the LEDs did not change with the prolongation of the detection time. Furthermore, there was no significant difference in time accuracy among the 4 μLEDs on the same MOSD II.

These findings suggested that the driver module of the FIMOSS implant can provide highly accurate optogenetic stimulation, offering precise and reliable optical stimulation for neuroscience experiments involving peripheral nerves.

Biocompatibility of long-term FIMOSS implantation in mice brachial plexus

Good biocompatibility was a crucial prerequisite for the application of FIMOSS. We implanted FIMOSS into the brachial plexus of mice and conducted behavioral tests 12 weeks after implantation surgery (Fig. 4a). The mice were divided into four groups: Control group and upper trunk/middle trunk/lower trunk implantation group. After the behavioral tests, we performed immunofluorescence staining on the nerve trunks at implantation site of MOSD II.

We performed the motion analysis experiment to quantitatively evaluate the range of motion of multiple joints of forelimbs in free-moving mice. Figure 4f, g shows representative movement trajectories of the forelimb from mice without FIMOSS implant (control group) and the implanted forelimb from mice with FIMOSS implant (implanted group), respectively. As a result, no significant difference was observed in range of motion of shoulder, elbow, wrist, and MP joints in forelimb between groups (Fig. 4h–k). We also assess motor impairments following FIMOSS implantation by catwalk gait analysis system (Fig. 4l, m). Stride length, print areas, stance time, swing time, and base of support have been reported to highlight the effects of peripheral nerve injury[32], but mice of three implantation group show no motor impairments with significant differences in these indicators (Fig. 4n–r). If FIMOSS implant or the implantation surgery could damage the brachial plexus, mice in different groups would have different performance of motor function deficit. However, the statistical results of these behavioral tests indicated that motor function of mice was not affected.

After the behavioral tests, we reopened the original incision as the implantation surgery. A thin layer of connective tissue could be observed encapsulating the FIMOSS Implant, with no significant abnormalities in the texture or structure of the pectoralis major muscle (Fig. 4b). The PDMS encapsulation of FIMOSS implant was intact. Around the brachial plexus, scar tissue was seen encapsulating the MOSD II, without noticeable inflammatory exudate or infectious tissue. Following the removal of MOSD II and the transection of scar tissue, the continuity and texture of the nerve appeared normal without any evident abnormalities (Fig. 4c).

Then we performed immunofluorescence staining on the middle trunks at implantation site and distal site of MOSD II along with upper trunks and lower trunks adjacent to the MOSD II (Supplementary Fig. 9e). And the myelin sheath at the implantation site was calculated to evaluate whether nerve compression had happened. As a result, the myelin sheath at the implantation site of MOSD II was normal, orderly distributed (Fig. 4d). And there is no significant difference in myelin sheath thickness compared with control group (Supplementary Fig. 9f). And there were almost no obvious inflammatory cells between the perineurium. Moreover, myelin sheath of the middle trunks distal to MOSD II implantation site and the adjacent upper and lower trunks (Supplementary Fig. 9a–d) were also without obvious abnormalities. Only a few inflammatory cells could be seen in the connective tissue surrounding the epineurium.

In conclusion, our results showed that the function of forelimb on the implanted side was not significantly different from that of mice in control group, indicating that FIMOSS implants have good biocompatibility because the free moving of the implanted mice and the normal function of the implanted brachial plexus were not affected.

Distinct forelimb movements induced by FIMOSS

After exiting the intervertebral foramina, spinal nerves intertwine to form networks known as peripheral nerve plexuses. In mice, these nerve plexuses include the cervical, brachial, lumbar, and sacral plexuses. Among them, brachial plexus is particularly significant as it is responsible for complex sensorimotor functions of the forelimb, so we applied FIMOSS on brachial plexus as a representative of peripheral nerve plexus (Fig. 5a, b).

The FIMOSS implants were activated using FIMOSS external device when the mice were anesthetized with isoflurane (Fig. 5c), and all the experiments were carried out 12 weeks after the implantation surgeries, when the incision was healed (Fig. 5d). Thy1-ChR2-EYFP mice were divided into three groups, with the MOSD II of FIMOSS implants interfacing with the upper trunk (Fig. 5e), middle trunk (Fig. 5f), and lower trunk (Fig. 5g), respectively. CMAP of biceps brachii, triceps brachii, forearm extensors and forearm flexors were recorded when μLEDs from different angles on the MOSD II was turned on, respectively (default wireless condition) (Fig. 5k). Simultaneously, a high-speed camera was used to record the distinct forelimb movement induced by FIMOSS, and Deeplabcut Toolbox was employed for pose estimation of forelimbs afterwards (Fig. 5l).

Firstly, we stimulated middle trunk as a representative nerve with different pulse width (5, 10, 20, 30, 40 ms) to determine appropriate parameter to induce forelimb movement and record CMAP curve. The results indicated that the pulse width of 20 ms was sufficient to induce obvious CMAP curve recorded from forearm extensors (Supplementary Fig. 10a, c) and triceps brachii (Supplementary Fig. 10b, d), with obvious wrist extension (Supplementary Fig. 10e, g) and elbow extension (Supplementary Fig. 10f, h) being induced at the same time. So, a pulse width of 20 ms was selected for further experiments. This can be attributed to several action potentials generated at the targeted nerve fascicles, which induced more obvious angle changes.

When MOSD II was implanted onto upper trunk, we observed that elbow flexion (Fig. 5m) and wrist extension (Fig. 5n) were respectively induced by different angles, which was mainly attributed to the activation of biceps brachii innervated by musculocutaneous nerve and brachioradialis as well as extensor carpi muscles innervated by partial branches of radial nerve derived from the upper trunk. Figure 5h showed the relationships between the induced forelimb movements, the CMAP area and the position of the μLEDs. In detailed, LED2 elicited typical movements of elbow flexion with a significant larger CMAP area recorded from biceps brachii compared with LED1,3 and 4. While LED3 elicited wrist extension with a largest CMAP area recorded from forearm extensors. LED1 elicited elbow flexion with a relatively small angle and CMAP area recorded from biceps brachii. When LED4 were turned on, no typical movements were observed, and relatively small CMAP area was recorded from all the four muscle groups.

As for the middle trunk (C7 nerve), multisite optogenetic stimulation mainly induced the contraction of triceps brachii (Fig. 5o) or forearm extensor muscles (Fig. 5p). As illustrated in Fig. 5i, LED1 exhibited a tendency to induce the extension of wrist and MP joints with the largest CMAP area recorded from forearm extensors. LED3 typically induced elbow extension, with a significant CMAP area from triceps brachii was recorded compared with those from forearm extensors, flexors, and biceps brachii. Weak CMAP area were recorded from different muscle groups when LED2 and LED4 were turned on, respectively. We assumed that an extremely small quantity of motor axons within middle trunk were directly against by these two LEDs resulting in no movements observed with limited CMAP area recorded.

Optogenetic stimulation of lower trunk could commonly induce elbow extension, flexion or extension of wrist and finger abduction (Fig. 5q-s), respectively. However, under the same optical power of optogenetic stimulation, lower trunk stimulation exhibited a tendency to induce more obvious wrist and finger movement compared with middle trunk. Figure 5j showed the detailed results of electrophysiological and induced-behavioral tests. LED1 induced wrist and MP joint flexion with a larger CMAP area recorded from forearm flexors. LED2 induced typical movements of fingers abduction with MP joint extension. The lighting of LED3 selectively elicited elbow extension with an obvious CMAP amplitude recorded from triceps brachii. LED4 induced no obvious forelimb movements and CMAP area recorded.
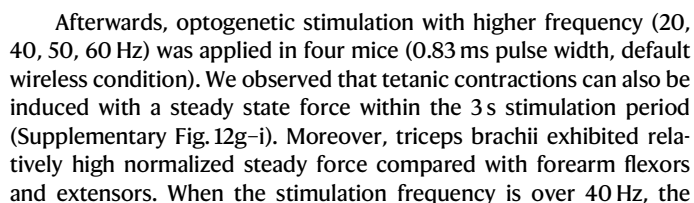
Furthermore, to clarify the characterization of optogenetic stimulation by FIMOSS, we systematically compared the induced movements between multisite optogenetic (20 ms pulse width, default wireless condition, $n = 6$) and electrical stimulation (single-site, 0.2 ms pulse width, 0.5 mA current intensity, $n = 6$). As a result, both electrical stimulation and multisite optogenetic stimulation at brachial plexus could effectively induce obvious elbow joint movement (Supplementary Fig. 11a-c). However, the relatively low spatial resolution of electrical stimulation limited its function in selective activation of distal forelimb joints (Supplementary Fig. 11g-i). The angle changes of wrist and metacarpophalangeal joints were often obscured by concomitant elbow movement, manifesting as low-amplitude oscillations in joint angle measurements in these joints (Supplementary Fig. 11d-f). These elbow motion-associated wrist/hand movements cannot serve as valid metrics for evaluating wrist and hand motor movements. In contrast, multisite optical stimulation induced selective activation of wrist and metacarpophalangeal joints with minimal elbow involvement, which indicated that the observed joint movements resulted from direct muscle contractions rather than being kinematic artifacts of proximal joint movement.

In conclusion, our experiments showed that the 4 μLEDs of FIMOSS implants surrounding the nerve trunk could successfully activate different nerve fascicles within a single nerve with high selectivity, thereby inducing different movements of forelimbs. Both induced-behavioral and electrophysiological results demonstrate the high spatial selectivity of FIMOSS compared to electrical stimulation. Moreover, these results suggested that FIMOSS is finely tuned to the functional anatomical characteristics of the brachial plexus in mice, which has been reported in previous studies[31].

Distinct muscle contractions induced by FIMOSS

In previous study, muscle contraction of distinct hindlimb can be induced by optogenetic stimulation at stem cell−derived motor neurons engrafted on the sciatic nerve[33] or nerve branches from sciatic nerve[34]. And yellow-green laser (561 nm) at sciatic nerve can reversibly inhibit twitch and tetanic muscle force induced by electrical stimulation in Thy1::eNpHR2.0 mice[35]. To test whether multisite optogenetic stimulation of FIMOSS implants on brachii plexus can induce twitch or tetanic muscle contraction of different forelimb muscle groups, we conducted the isometric muscle tension physiology experiment.

We used the lower trunk as a representative nerve. A FIMOSS implant was implanted on the trunk and activated by an external device. Firstly, we conducted distinct movement induction to clarify the correspondence between different μLEDs and muscle groups innervated by lower trunk. In a representative Thy1-ChR2-EYFP mouse, wrist extension, wrist flexion, and elbow extension were respectively induced by the illumination of μLED1, μLED2, μLED4. No obvious movement can be observed when illuminating μLED3 (Supplementary Fig. 12a, b). Then the distal tendons of the triceps brachii, forearm flexors, and forearm extensors were severed and connected to a force transducer. μLED4 was continuously (1 Hz, 20 ms pulse width) illuminated to induce twitch contractions in the triceps brachii (Supplementary Fig. 12c), while μLED2 and μLED1 were used to induce twitch contractions of the forearm flexors (Supplementary Fig. 12d) and forearm extensors (Supplementary Fig. 12e), respectively. Distinct forelimb muscle groups showed different twitch force when illuminating lower trunks with different μLEDs (Supplementary Fig. 12f).

Afterwards, optogenetic stimulation with higher frequency (20, 40, 50, 60 Hz) was applied in four mice (0.83 ms pulse width, default wireless condition). We observed that tetanic contractions can also be induced with a steady state force within the 3 s stimulation period (Supplementary Fig. 12g–i). Moreover, triceps brachii exhibited relatively high normalized steady force compared with forearm flexors and extensors. When the stimulation frequency is over 40 Hz, the normalized steady force began to decrease obviously (Supplementary Fig. 12j–l).

In conclusion, both twitch or tetanic contraction of distinct forelimb muscle groups can be induced by FIMOSS implants. Among different forelimb muscles, the twitch force and normalized steady force profiles exhibited variations both in the magnitude of muscle force and the rate/degree of muscle fatigue. Moreover, when the

Fig. 5 | The application of FIMOSS on brachial plexus to induce distinct movements of forelimb in mice. a An operative microscope photograph of the brachial plexus of a mouse: C5 (**a**) and C6 (**b**) nerve root merge to form upper trunk (**c**); middle trunk (**d**); lower trunk. (scale bar = 500 μm) **b** A diagram of brachial plexus structure. **c** The activation of FIMOSS implant with an external device. (scale bar = 1 cm) **d** Healed surgical incision 2 weeks after implantation. (scale bar = 500 μm) Intraoperative photographs of MOSD II interfacing with upper trunk (**e**), middle trunk (**f**), lower trunk (**g**). (scale bar = 500 μm) **h–j** Circular statistical graph of representative CMAP area (mV*ms) from target muscles and angle changes (°) of distinct forelimb movements induced by different μLEDs (20 ms pulse width, 2000 ms inter-pulse interval, default wireless condition) during multisite optogenetic stimulation of upper trunk (**h**), middle trunk (**i**), and lower trunk (**j**). BC, biceps brachii. TC, triceps brachii. FE, forearm extensors. FF, forearm flexors.

HIM, hand intrinsic muscles. MP joint, metacarpophalangeal joint. **k** Schematic of CMAP recording experiment set-up. The CMAP of biceps brachii, triceps brachii, forearm flexors and forearm extensors were recorded. **l** Schematic of angle analysis experiment set-up. Angle changes of shoulder (purple), elbow (blue), wrist (green), metacarpophalangeal joint (orange), fingertips (red) were calculated with the pose estimation of these joints using Deeplabcut Toolbox. **m–s** Representative kinematic trajectory of mice forelimb elicited by FIMOSS implant. S, shoulder. E, elbow. W, wrist. M, metacarpophalangeal joint. F, fingertips. Multisite optogenetic stimulation of upper trunk can induce wrist extension (**m**) or elbow flexion (**n**), while that of middle trunk can induce elbow extension (**o**) or wrist extension (**p**). Lower trunk is mainly responsible for wrist extension with finger abduction (**q**), elbow extension (**r**) and wrist flexion (**s**). Corresponding CMAP curves of various forelimb muscle groups were shown, respectively, on the right.
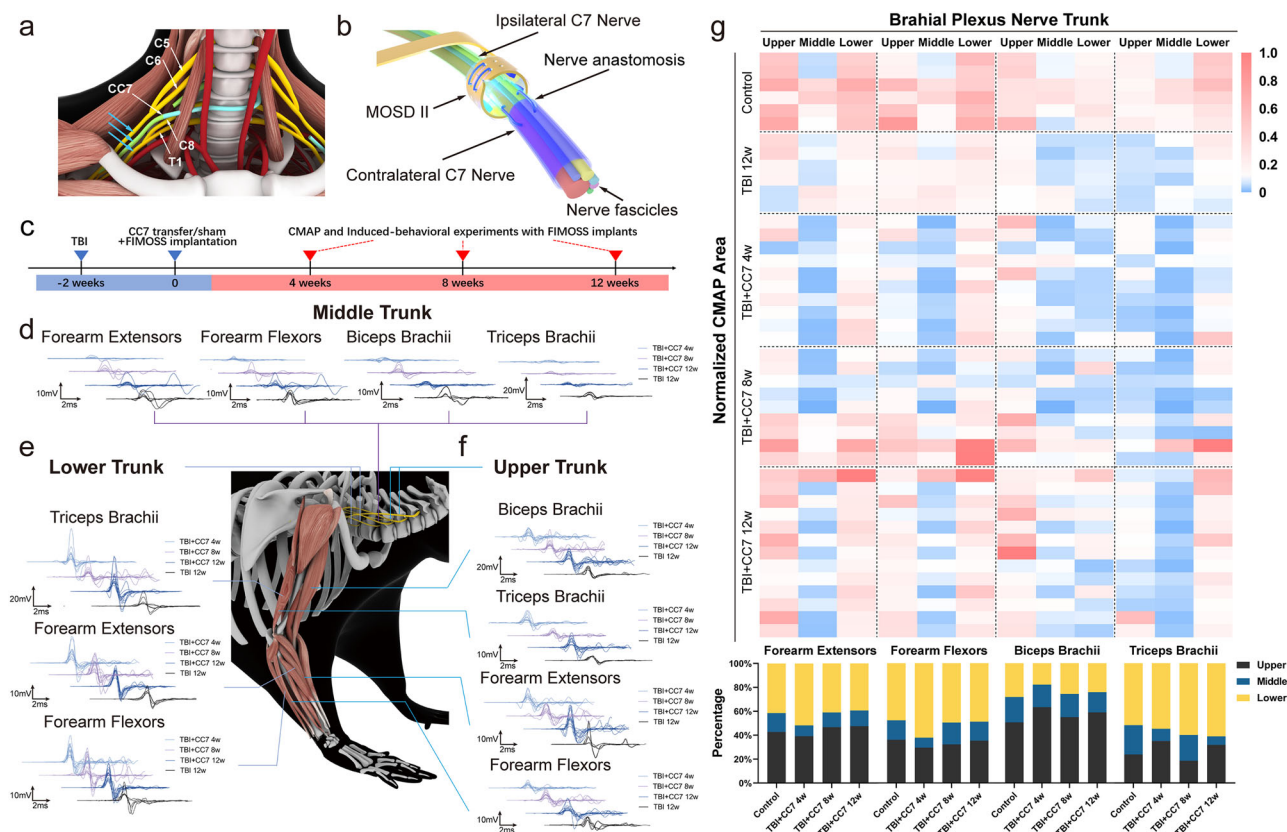
Fig. 6 | Electrophysiology change pattern of brachial plexus after CC7 transfer evaluated by multisite optogenetic stimulation method. a A schematic diagram of CC7 transfer surgery. Upper trunks and lower trunks were marked yellow. Middle Trunks of healthy side and impaired side were marked cyan and green, respectively. The implantation positions of the MOSD II were pointed by blue arrows. **b** Schematic of the strategy of CMAP experiments by MOSD II. MOSD II was wrapped around the transferred C7 nerve and fixed on the distal (green) of nerve anastomosis by microsutures. Different nerve fascicles were illustrated in different colors. **c** Timeline of CMAP and induced-behavioral experiments after TBI and CC7

transfer. CMAP curve of forearm extensors, forearm flexors, biceps brachii and triceps brachii induced by spatially selective optogenetic stimulation of regenerating middle trunks (**d**), lower trunks (**e**) and upper trunks (**f**). CMAP curves from each mouse in TBI + CC7 groups (mice undergoing TBI and CC7 surgery) at 4, 8, and 12 weeks after surgery and TBI groups at 12 weeks after surgery were presented. **g** The heatmap of CMAP area from different mice groups and weighted analysis of brachial plexus innervation to four muscle groups on the affected limb. $n = 6$ for control and TBI 12w group, $n = 10$ for TBI + CC7 4w group, $n = 9$ for TBI + CC7 8w group, $n = 13$ for TBI + CC7 12w group.

stimulation frequency rose from 0 to 60 Hz, the normalized steady force demonstrated an obvious decrease over 40 Hz. These results aligned with previous studies. The frequency limit can be attributed to the desensitization of ChR2[34,36].

Electrophysiological changes of brachial plexus evaluated by FIMOSS stimulation after CC7 transfer

Clinical trial[7] and animal experiments[19] have proven that CC7 transfer (Fig. 6a) improve the function of affected forelimb after TBI, which was attributed to the sprouting of contralateral corticospinal tract fibers to the ipsilateral affected side in the spinal cord. Although segments

innervating the brachial plexus ranging from C5 to T1 have proven to be involved in this process, the contributions of different nerve trunks at level of the brachial plexus to function recovery remained unknown. Based on FIMOSS's capability of spatially selective optogenetic stimulation, we explored the function change pattern of different nerve fascicles in brachial plexus nerve trunks at 4 weeks, 8 weeks, and 12 weeks after CC7 transfer/sham surgery (Fig. 6b, c).

As for the transferred C7 nerve (middle trunk), recorded CMAP areas of biceps brachii, triceps brachii, forearm flexors, and extensors were gradually increasing from 4 to 12 weeks post-operation (Fig. 6d). Among this CMAP areas of biceps brachii, forearm extensors, and

forearm flexors were not significantly different from the control group at 4 weeks and 8 weeks post-operation, with a further improvement observed at 12 weeks post-operation. Surprisingly, CMAP areas of triceps brachii was relatively weak compared with those of forearm extensors or flexors. In comparison, recorded CMAP area of triceps brachii when stimulating both upper trunk and lower trunk (Fig. 6e, f) exhibited a tendency of continuous increase, especially between 8 and 12 weeks after CC7 transfer. In addition, CMAP areas of upper trunk to biceps brachii and those of lower trunk to triceps brachii gradually recovered from 4 to 12 weeks post-operation. At the same time, the magnitude of CMAP areas recorded in forearm extensors and flexors were increasing when stimulating upper trunk or lower trunk, especially between 8 and 12 weeks.

The heatmap showed the comparison between CMAP area magnitude of different brachial plexus trunks recorded from four muscle groups in forelimb. (Fig. 6g top) And weighted analysis of electrophysiological results of brachial plexus nerve trunks to different forelimb muscle groups showed the functional compensation of upper and lower trunk to four muscle groups in forelimb in the time course of 12 weeks (Fig. 6g bottom).

In summary, our device enables accurate detection of CMAP of different nerve fascicles to distinct muscle groups with spatially selective optogenetic stimulation. The electrophysiology changes of brachial plexus after CC7 transfer implied that although transferred C7 nerve participated in the innervation of various forelimb muscle groups, it played a more important role in the reinnervation of the wrist and hand muscles on the affected side. Meanwhile, the upper trunk showed a tendency to innervate the triceps brachii with a higher proportion, which was mainly controlled by C7 nerve and lower trunk in control group. Both the upper and lower trunk were compensating for the innervation of forearm extensors and flexors, which is responsible for the motor control of wrist and hand. As a consequence of the motor function reorganization in brachial plexus, TBI + CC7 group demonstrated significantly better CMAP results compared with TBI group after 12 weeks.

Changes in distinct movements induced by FIMOSS stimulation after CC7 transfer

To study the reinnervation of distinct forelimb muscles by the transferred C7 nerve and the changes in the innervation by upper and lower trunks after CC7 surgery, we applied the FIMOSS system on different nerve trunks in the brachial plexus to detect subtle changes in induced-behavioral results of different nerve fascicles during the process of transferred C7 nerve regeneration within 12 weeks.

Regarding the regenerating C7 nerve, an increasing variety of movements can be induced from 4 to 12 weeks post-operation (Fig. 7a–e, kinematic trajectories in Fig. 7f), among which elbow movements appeared in all mouse models from 4 weeks post-operation, and wrist movements was emerging in mouse models after 4 weeks post-operation, with a further increase in frequency at 8 and 12 weeks after operation (Fig. 7g). Furthermore, mean angle changes of these movements increased generally with the extension of postoperative time. Surprisingly, C7 nerve-elicited wrist flexion, which was not a major induced movements in control groups, appeared more frequently in TBI + CC7 groups after 8 weeks post-operation (Fig. 7h right). However, despite the fact that the transferred C7 nerve can induce various movements, including elbow extension, elbow flexion, wrist extension, wrist flexion and finger extension at 12 weeks post-operation, angle changes of these joints were smaller compared to the induced movements of the upper and lower trunk (Fig. 7g–j).

As for upper trunk and lower trunk, angle changes of various movements, which was primarily controlled by upper and lower trunks gradually recovered, especially from 8 to 12 weeks. These movements include upper trunk-elbow flexion (Fig. 7i left), lower trunk-wrist flexion (Fig. 7j middle) and lower trunk-finger flexion (Fig. 7j right).

Additionally, angle change of upper trunk-wrist extension (Fig. 7i right) and lower trunk-elbow extension (Fig. 7j left), which were not primarily controlled by these nerve trunks, gradually increased from 4 to 12 weeks post-operation. Except angle changes in elbow and wrist movements, changes in fine movements of forelimb can also be observed. Finger abduction, controlled by the ulnar nerve branched from lower trunk, tended to be induced more frequently in TBI + CC7 groups with the extension of postoperative time, which can be induced in all mice in the control group and at a relatively lower percentage in TBI groups (Fig. 7k).

Together with the quantitative results from induced-behavioral experiments, FIMOSS selective stimulation on brachial plexus confirmed that the transferred C7 nerve reinnervated various muscle groups in the affected forelimb after TBI. Meanwhile, the function of upper and lower trunk was improving and compensating the function of C7 nerve along with the regeneration of C7 nerve, exhibiting the functional reorganization of the brachial plexus after CC7 transfer.

Discussion

Several advanced optogenetic devices with diverse advantages have been reported recently. Latest advancements have achieved features such as fully implantable designs[37], absorbability[38], programmability[39], and closed-loop control with concurrent electromyographic monitoring[40–43]. The intervention sites range from central to peripheral nervous systems, including the brain[44–46], spinal cord[41,47,48], and peripheral nerves[40,49,50]. Many recent reports of wireless and battery-free optogenetic devices showcased the applications in freely-moving animals[51–57]. Optogenetic studies in freely moving animals expand experimental design's possibilities while benefiting animals and researchers by eliminating fixation or anesthesia. Therefore, one future direction of the FIMOSS implant is to explore compatibility with a commercially available RF driver (NeuroLux, Inc.) to enable wireless operation in freely-moving conditions. The NeuroLux wireless system is capable of driving a much larger emitting coil that surrounds and provides wireless power to an arena size up to 70 cm by 70 cm[52].

In order for FIMOSS implant to operate in larger arena sizes, the energy harvesting capability of the receiving (secondary) coil needs be improved by increasing its mutual inductance with the emitting (primary) coil (M_{21}). The mutual inductance scales positively with the number of turns of the secondary coil (N_2) and the magnetic flux through the secondary coil from primary coil (Φ_{21}) (Eq. 1). Therefore, one can increase N_2 or coil area A_2 for a more robust energy harvesting capability.

$$M_{21} = \frac{N_2 \Phi_{21}}{i_1}, where \; \Phi_{21} = B_{21} A_2 \cos\theta_{21} \tag{1}$$

In this study, we advanced the previously reported MOSD into FIMOSS (a flexible, integrated, and miniaturized system for multisite optogenetic stimulation). The purpose of developing this system is to achieve long-term follow-up and self-control study of both electrophysiology and induced-behavioral experiments in mice. Our FIMOSS system can avoid potential injury to the targeted nerve due to repeated surgeries, which can be an issue in the previous version of FIMOSS, namely the acutely implanted device MOSD[22]. More importantly, since many muscles are jointly controlled by multiple nerve trunks, sometimes the proportion varies significantly among individuals. For example, triceps brachii is innervated by the radial nerve, which receives contributions from the upper, middle, and lower trunks of the brachial plexus (Fig. 5b). Although the middle and lower trunks typically dominate its control, significant individual variations exist between their relative contributions (Fig. 7g, j). Our system achieves long-term follow-up and self-control study of both electrophysiology and induced-behavioral experiments in mice, which can detect subtle changes in nerve functions with sub-nerve resolution.
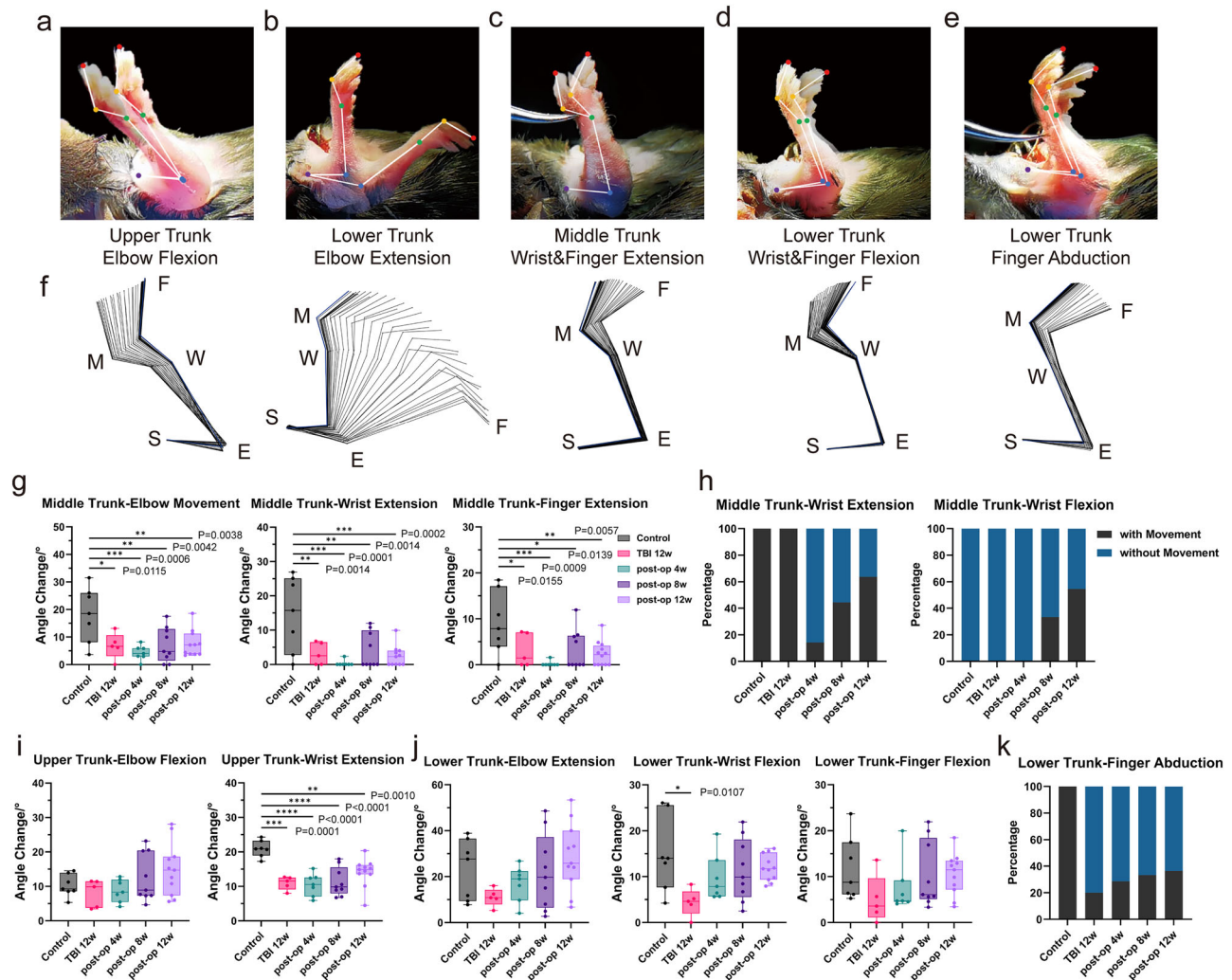
Fig. 7 | Induced-behavioral changes of impaired forelimb after CC7 transfer. Representative image of induced movements including the flexion and extension of elbow (**a**, **b**), wrist, fingers (**c**, **d**) and finger abduction (**e**). **f** Corresponding forelimb movement trajectory with the position of shoulder (S), elbow (E), wrist (W), metacarpophalangeal joint (M), fingertips (F) marked. **g** The maximum angle changes of induced movements when different μLEDs illuminated middle trunk (transferred C7 nerve). **h** The number of mice that successfully elicited wrist extension or wrist flexion when illuminating middle trunks with MOSD II as a percentage of the total number of mice in different groups. **i**, **j** The maximum angle changes of induced movements when different μLEDs illuminated upper trunk (**i**) and lower trunk (**j**). **k** The number of mice that successfully elicited finger abduction when illuminating lower trunk with MOSD II as a percentage of the total number of mice in different groups. The boxplots in **g**, **i**, and **j** show the median (center line), the 3rd and 1st quartiles (upper and lower bounds of the box, respectively). The whiskers represent the maximum and minimum values, respectively. $n = 7$ for control group, $n = 5$ for TBI 12w group, $n = 7$ for TBI + CC7 4w group, $n = 9$ for TBI + CC7 8w group, $n = 11$ for TBI + CC7 12w group in (**g**–**k**). *$P < 0.05$, **$P < 0.01$, ***$P < 0.001$, one-way ANOVA and multiple comparison tests with Dunnett's correct in (**g**–**k**).

Previously-reported optogenetic stimulation devices designed to regulate peripheral nerves often use the rat sciatic nerve as a representative nerve[58,59]. However, these designs may not always meet the experimental requirements, especially when targeting deeper-seated nerves such as the brachial plexus or lumbosacral plexus. On one hand, the deeper-seated nerves often exhibit significant scar hyperplasia and adhesion once exposed surgically. On the other hand, device implantation to the brachial plexus nerve in mice poses more challenges due to its intricate proximity to the subclavian artery and venous sinus, coupled with a minute nerve diameter ranging from 300 to 400 μm. Consequently, re-exposure surgery can be highly intricate or even destructive to the nerves. In our study, we have also tried to re-expose the brachial plexus and conduct the electrophysiological and induced-behavioral experiments repeatedly with acutely implanted MOSD at 8 weeks or 12 weeks in mice that had experienced experiments at 4 weeks after CC7 transfer. However, the surgery resulted in major adverse events because of the adhesion between brachial plexus,

subclavian artery, and venous sinus (data not shown). Even if re-exposure can be accomplished without impairment to these structures, the process of scar resection and neurolysis may inevitably lead to neural tissue damage and nerve traction. Hence, FIMOSS allowed the evaluation of the functional changes of brachial plexus at multiple time points, which is not possible using MOSD.

Our experiments have demonstrated that FIMOSS maintains the selective activation advantage of MOSD and has been further optimized for standardized and batch production. The MOSD II structure, with its wider profile compared to the relatively narrow polyurethane fiber in MOSD, reduces the risk of nerve compression. These advantages make FIMOSS a reliable and novel experimental tool for application in electrophysiological experiments for mice or other larger animal models. Additionally, attribute to the function of FIMOSS reprogramming and multisite optogenetic stimulation, we could successfully induce multiple movements of brachial plexus, including flexion and extension of elbow, wrist, and fingers, and abduction of

fingers. Therefore, we can dynamically observe the functional recovery of nerve fascicles that innervate different muscle groups through quantitative assessment of induced movements. This concept represents a new approach to evaluate the function of peripheral nerve with high spatial resolution, particularly in decoding complex nerve structures like the brachial plexus or the lumbosacral plexus. Traditionally, achieving selective muscle control needs complex retrograde tracing of different muscles using viruses, which was often complex in practice and resulted in incomplete transduction. Previous studies achieved focused motor control via optogenetic/intramuscular electrical stimulation, minimizing off-target muscle activation[60,61]. Direct muscle stimulation offers applicability for denervated or single-target muscles[62–65] with simpler surgical access but incurs unnatural synchronous contraction and limited activation of thick muscles due to inadequate light penetration. In contrast, indirect fascicular stimulation leverages physiological recruitment order for graded force and fatigue resistance while enabling coordinated multi-muscle activation through selective neuromodulation[22,66]. However, this approach requires an intact motor pathway, necessitates complex neural interfaces with sub-nerve resolution, and involves intricate implantation surgery near critical neurovascular structures. Our system bridges this specificity-invasiveness gap, providing multi-muscle control while preserving physiological recruitment patterns. Despite brachial plexus trunks mentioned in our study, radial nerve[67,68], median nerve[11,69,70], and ulnar nerve[71,72] in the forelimb also serve as ideal target nerves due to their composition of more than four nerve fascicles. They control the extension of elbow, the rotation of the forearm, the flexion/extension/rotation of wrist, as well as flexion/extension/adduction/abduction of each finger intricately and precisely.

Recent studies have shown that epidural electrical stimulation can restore motor function in paralyzed patients and monkeys, which has realized the recovery of spinal cord injury and achieved excellent clinical translation[66,73,74]. From the perspective of the hand surgery department, our experiments suggest that targeted neuromodulation of the brachial plexus has the potential to control various upper limb movements with a smaller incision and simpler implantation surgery. Given the risk of nerve damage associated with spinal surgery itself, brachial plexus neuromodulation could be safer and as effective as epidural stimulation. In our behavioral experiments, employing a prolonged 20 ms stimulus effectively induced distinct forelimb movements. We attributed this to repetitive action potential firing within the targeted nerve axons, which generated significantly greater joint angle changes than a single twitch but also led to rapid muscle fatigue. But in muscle contraction experiments, we utilized 0.83 ms pulses with high frequency, thereby inducing sustained, fatigue-resistant contractions. Based on these results, we demonstrated the potential for achieving precise control of coordinated multi-muscle forelimb movements. Our system provides the possibility of long-term implantation, and further experimental exploration is required to explore other application[75].

It is worth noting that the foundation of FIMOSS design is FPC preparation technology. We applied a 65 μm substrate with 12 μm Parylene C and 200 μm PDMS encapsulation, with the interconnect only encapsulated by PDMS, to ensure miniaturization and flexibility while guaranteeing effective encapsulation. However, its flexibility is still inferior to other advanced flexible materials, making it possible to restrict the movement of forelimbs in mice if the interconnects were implanted across the wrist or elbow joints. To minimize device damage from mouse movement, Liu et al. reported a motion-adaptable semi-implantable hydrogel optical fiber system recently, which provided diverse peripheral nerve neuromodulation with different wavelengths and does not restrict the natural motion of mice[76]. Unlike the application of flexible hydrogel fiber, we avoided this problem by implanting the MOSD II interface at the brachial plexus, which does not experience significant bending or displacement during natural motion

in mice. However, a degradable and flexible MOSD II is still a more suitable solution for optogenetic stimulation of peripheral nerve in distal forelimbs and clinical translation. Therefore, future optimization will involve applying more advanced materials to replace the FPC substrate, including more flexible materials such as hydrogels[76,77] or degradable materials[39,58,78,79].

Methods

Fabrication of FIMOSS implant electronics
The global trace width and clearance were 2.5 mil/2.5 mil. As illustrated in Supplementary Fig. 13a, the PCBA of the FIMOSS implant was fabricated by commercially available PCBA manufacturer. Each panelized FPC board was fabricated and assembled, containing 40 units of the FIMOSS implant circuit board. The units that passed functional validation were severed from the panelized FPC, and FIMOSS implant firmware was uploaded to the MCU (STM8L101F3U6TR, STMicroelectronics) onboard the FPC units (Supplementary Fig. 13b). The programmed units were then immersed in ethanol absolute and placed in ultrasonic cleaner to be cleaned at rooms temperature (25 °C) for 3 min (Supplementary Fig. 13c).

Encapsulation of FIMOSS implant
The driver region of the cleaned FPCs, as highlighted in blue in Supplementary Fig. 13d, were coated with Parylene C (thickness,12 μm) through chemical vapor deposition (CVD). The coated FPCs then underwent plasma treatment to improve bonding between the FPC surface with the upcoming encapsulation substrate (polydimethylsiloxane, PDMS).

A set of stainless-steel molds, designed for the encapsulation process, were used to further encapsulate the FPC units with PDMS (Sylgard 184, Dow Corning). The mold cavity was designed to take the exact shape of the FPC but expanded 500 μm on all dimensions of the original shape. The mold consists of the upper die, the lower die and two position pillars. The encapsulation process began with placing the lower die and the upper die on flat surface, and apply PDMS mixture (A:B = 12:1, well-mixed, de-aired by vacuum chamber) to fill half depth of all 10 cavities on each die. Both the lower die and the upper die were then transferred to oven to cure the PDMS at 120 °C for 20 min (Supplementary Fig. 13e). Once the dies were taken out and cooled, 10 FPC units were placed in each cavity of the lower die. The FPC units were fixated to the cavity by applying a few drops of PDMS mixture to connect the FPC with the stainless-steel cavity and cured at 85 °C for 20 min (Supplementary Fig. 13f). After fixation of the units, completely fill all the cavities of the lower and the upper die with PDMS mixture. The lower die was placed on a flat surface with the cavity facing up, and the two position pillars were inserted in the corresponding sockets. The upper die was then lowered and pressed onto the lower die while aligning through the position pillars (Supplementary Fig. 13g). 4 screws on each corner of the mold set, together with a pressure clamp were used to firmly enclose the two dies together. And the enclosed mold was cured at 85 °C for 6 h. After the curation, the mold was cooled to room temperature and opened to remove the encapsulated devices from the cavities (Supplementary Fig. 13h).

Lastly, the encapsulated devices were cleaned of residuals and debris by using tweezers to remove the flashes (excessive material attached to a molded product), and by ultrasonic cleaning (immersed in ethanol absolute, at 25 °C, 3 °C). The cleaned encapsulated devices were placed on a glass slide, with the flexible interconnect and the cuff region residing outside of the edge of the slide to maintain not in contact with the slide (Supplementary Fig. 13i). And depending on the size of the nerve that this batch of devices were targeting, the devices can either go through a non-sacrificial encapsulation process for the interconnect and MOSD II (Supplementary Fig. 13cj–m) to accommodate for bigger nerves ($d = 600$ μm, Fig. 2h), or a sacrificial pre-curling encapsulation process (Supplementary Fig. 4) to better assist the implantation of the MOSD II in typical nerve sizes ($d = 380$ μm,

Fig. 2g). The pre-curling process involved sacrificing the outer two suture eyelets on each side of the cuff FPC, and therefore during the implantation, the inner eyelets would be used instead of the outer eyelets, to fully suture into a cuff. And thus, the resulting cuff diameter would be fit for a smaller nerve size than if the outer two suture were preserved. In short, the outer eyelets can either be used sacrificially to pre-curl an easy-to-implant nerve cuff, or be used non-sacrificially to extend the cuff diameter for larger nerves. The sacrificial pre-curling process was predominantly used to manufacture the FIMOSS implant devices in animal experiments reported in this article.

Wireless programming of FIMOSS implant

Wireless programming of the stimulation strategy stored on the FIMOSS implant can be done before and after the implantation. Firstly, the FIMOSS external device was connected to a DC power source (3.3 V, 200 mA current limit) and to a computer via a USB-TTL dongle (CH340G). On the computer, an open-source serial communication software (XCOM V2.0) was used to transmit the programming command string to the MCU (ATMEGA328PB-MU, Microchip Technology, USA) at a baud rate of 9600 via the USB-TTL dongle. Before a programming session, the operator should construct the desired command string by consulting the stimulation parameter look-up table (Supplementary Tables 1–3), and load the string to be sent on the serial communication software. During a programming session, the user first switch on the DC power supply, thus activating the FIMOSS external device to emit wireless power. Then, the external antenna was brought close to the receiving antenna of the FIMOSS implant (the antenna pair should be concentric and parallel with each other, at a parallel distance of ~1 mm) to power the implant. If implant was checked to be correctly powered, by observing the blue status LED on the driver region of the implant being illuminated, and within 2 s window starting from the boot up of the implant, the operator should click "send" on the serial communication software on the computer, to transmit the command string. The success of the wireless programming operation was confirmed by the blue status LED flashing in a rapid pattern (Supplementary Movie 2).

Fabrication and firmware programming of FIMOSS external device

The hardware of a FIMOSS external device was assembled from the PCBA, and a pair of 3D-printed case. The PCBA was manufactured by commercially available PCBA manufacturer (JLCPCB, China). The PCBA was placed within its designated compartment between the 3D-printed case (Supplementary Fig. 5). The firmware was written and tested on the Arduino IDE because the MCU onboard the FIMOSS external device was a similar variant of the MCU used in an Arduino Uno. To upload the firmware, an Arduino Uno was used as the in-system programmer (Arduino as ISP) to upload the compiled program to the external device.

COMSOL analysis of light propagation of the MOSD II

First, a 3D geometric model (Fig. 3k) was created in SolidWorks 2023 using dimensions specified in Fig. 3i. Then the geometry was exported as a STEP file and imported to COMSOL 6.3, and a 3D FEA study using the Helmholtz equation was set up. The Helmholtz equation (Eq. 2) was a widely accepted computational model to study light propagation in space[80,81], where c is the diffusion coefficient (1 m^{-1}) accounting for both scattering and absorption (Fig. 3i), a is the absorption coefficient (1 m^{-1}), and f is the source term (W m^{-3}), and u is the irradiance (W m^{-2}) in space. The optical parameters for the various transmission medium used in the study is specified in Fig. 3i[82,83]. The mesh was constructed using tetrahedral geometry, and with an element size of "extra fine".

All domains were initially set to have a source term equal to 0. To simulate 1 μLED emitting light at 2.5 mW of optical power, its corresponding LED domain was set to have a source term of 5.17E10 (W m^{-3}), which, when integrated across the LED's volume returned 2.5 mW.

Similarly, to simulate two neighboring μLED emitting light at a reduced optical power of 2.0 mW, each of their corresponding LED domain was set to a source term of 4.03E10 (W m^{-3}). A volume plot was used to visualize the 3D distribution of irradiance in the one-LED illumination case (Fig. 3k). From the 3D simulation datasets, a 2D cut plan was defined as the XY-plane slicing down the Z-direction, middle of the μLED to visualize the propagation of irradiance across the cross-section of the nerve (Fig. 3l, m). Lastly, the 2D cut plane datasets were used to evaluate the surface average irradiance in each of the eight nerve sectors (Fig. 3j).

$$\nabla \cdot (-c\nabla u) + au = f \qquad (2)$$

Implantation process of FIMOSS implant

After successfully inducing anesthesia using 1.5–2% isoflurane, the Thy1-ChR2-EYFP mice were placed in a supine position and fixed on the operating table. During the procedure, the concentration of isoflurane was maintained at 0.8–1%, and both forelimbs were fixed in a shoulder abduction position of 90°. The skin on the right forearm and right chest was depilated carefully and then disinfected with alcohol. An L-shaped incision was made from the middle of the right forearm to the right sternoclavicular joint and extending to the xiphoid process. The subcutaneous tissue was bluntly dissected, and saline-soaked cotton balls were used to keep the skin edge moist during the implantation process. The pectoralis major and pectoralis minor muscles were sequentially incised along the line extending from the intermuscular groove to expose the deep brachial plexus nerve branches. The cervical transverse artery, superficial to the nerve trunks, was cauterized and resected. A retractor was used to pull the venous sinus medially, exposing the three brachial plexus trunk branches. Skin flaps were used to bluntly expose the separated nerve trunks during the procedure.

Afterwards, the FIMOSS implant's driver and power coil were placed at the head end, and the flexible MOSD II was wrapped around the target nerve trunk. The two ends of the MOSD II were brought to the superficial aspect of the nerve firstly, and 11–0 prolene sutures were passed through the suture eyelets to shape and fix the MOSD II, ensuring proper contact between the MOSD II and the nerve. Next, the FIMOSS implant was flipped, with the sutured portion of the MOSD II placed on the deep aspect of the nerve, and the driver and coil were positioned on the appropriate surface of the ipsilateral thoracic cavity, ensuring that the MOSD II did not exert tension on the nerve trunk. The retractor was released, and the MOSD II was positioned on the deep aspect of the venous sinus. The interconnect was carefully bent to accommodate the anatomical structure of the brachial plexus in mice. The FIMOSS implants were then fixed to the mouse's chest using 11–0 Prolene sutures. The incisions in the pectoralis major and skin were sutured with 11–0 Prolene sutures. After the procedures above, No.2, No.3 μLEDs and the interconnect are always located on the ventral side of the mouse (as shown in Fig. 5e–g). And the implanted MOSD II will not rotate during free moving behaviors in mice. This stability is one important advantage we considered when making decisions on the implant location of FIMOSS. After disinfecting the skin incision with alcohol, the mouse was placed on a warming blanket until it regained consciousness.

Mice from all groups in Figs. 5 and 6 were implanted a FIMOSS implant to conduct electrophysiological and induced-behavioral evaluation. However, control group in Fig. 4 didn't have an FIMOSS implant.

Electrophysiological and induced-behavioral evaluation of brachial plexus

The FIMOSS implant was implanted on the brachial plexus in mice from all groups for 12 weeks. For mice from TBI or TBI + CC7 groups,

the implantation surgery was performed 2 weeks after TBI surgery (when performing CC7 transfer for TBI + CC7 groups). The CMAP curves were recorded when the FIMOSS implant was activated (20 ms pulse width, default wireless condition) to explore the change pattern of brachial plexus electrophysiological values and forelimb induced-behavioral angle changes. For mice in control and TBI group, the experiments were conducted 12 weeks after implantation. For mice in TBI + CC7 group, the experiments were conducted 4, 8, and 12 weeks after CC7 transfer/implantation surgery. And FIMOSS implants will not be surgically removed after the 4-week or 8-week postoperative evaluation after implantation surgery until the 12-week postoperative evaluation was finished.

The process of electrophysiological and induced-behavioral evaluation of the brachial plexus was as follows. The Thy1-ChR2-EYFP mouse was placed in a supine position on the operating table under isoflurane anesthesia as described in the implantation process. The stimulation parameters of the FIMOSS implant were set to sequentially illuminate 4 μLEDs, with a pulse width of 20 ms, followed by an inter-pulse interval of 2 s. Each stimulation cycle was separated by an interval time of 2 s. This procedure was repeated for three times. A high-speed camera was positioned at a fixed location on the mouse's lateral side to record the induced movements of the right forelimb. Among different forelimb movements induced by the 4 μLEDs, the three videos with the largest angle change of the target joint induced by a single μLED will be selected for subsequent angle analysis.

Next, 4 pairs of needle electrodes were inserted, respectively, into the tendons and muscle bellies of the biceps brachii, triceps brachii, forearm extensors, and flexors of the right forelimb, with a separate ground electrode inserted in the tail. CMAP responses were defined as a repeatable and typical two-phase curve along with visible target muscle contraction, which was induced by optogenetic stimulation of FIMOSS and recorded by the Medtronic KeyPoint Portable EMG device afterwards. Then, in the heatmap Fig. 5g top, we normalized the CMAP areas using the maximum and minimum values of target muscle groups using the following formula:

$$Normalized\ CMAP\ Area = \frac{Raw\ Area - Min(\text{Muscle})}{Max(\text{Muscle}) - Min(\text{Muscle})} \quad (3)$$

In the weighted analysis of brachial plexus in Fig. 5g bottom, we calculated the innervation percentage of target nerve trunk to target muscle groups from different mice groups using the following formula:

$$Percentage_{\text{Nerve}} = \frac{Mean(\text{Nerve})}{Mean(\text{Upper}) + Mean(\text{Middle}) + Mean(\text{Lower})} \times 100\% \quad (4)$$

In vivo muscle contraction physiology induced by multisite optogenetic stimulation on lower trunk

Thy1-ChR2-EYFP mice were deeply anaesthetized using isoflurane and an FIMOSS implant was implanted onto the lower trunk through standardized surgery process above. Then the 4 μLEDs were lighted up in sequence to find the corresponding relationship between different μLEDs and the induced contraction of triceps brachii and forearm flexors. The angle change of elbow and wrist was calculated by Deeplabcut Toolbox. Then the distal tendons of the triceps brachii and forearm flexors were exposed, severed and individually connected to a force transducer (IWorx Systems Inc. FT-302) with a 6−0 prolene suture. Then the μLEDs which can induce the largest angle change of elbow extension and wrist flexion was illumined to induce the contraction of triceps brachii and forearm flexors, respectively. The stimulation parameter was set to duration = 20 ms and inter-pulse interval = 980 ms to elicit twitch muscle contractions. Then repetitive

high frequency stimulation of 20 Hz, 40 Hz, 50 Hz, 60 Hz with 0.83 ms pulse width, stimulation duration = 3 s was conducted to explore whether tetanic muscle contraction can be elicited by multisite optogenetic stimulation. Measurements with identical stimulation parameters were repeated five times in four mice ($n = 4$). The muscle contraction signal was recorded through a data recorder (IWorx Systems Inc. IX-214) and Labscribe software (IWorx Systems Inc.). Peak force is the maximum for each force profile within the 3 s stimulation duration. And steady state force was identified as the average of 1 s window before the end of 3 s stimulation duration. Normalized force in Supplementary Fig. 11g–i (Eq. 5) and normalized steady force in Supplementary Fig. 11j–l (Eq. 6) was calculated according to the equations below:

$$Normalized\ Force = \frac{Force}{Peak\ Force} \quad (5)$$

$$Normalized\ Steady\ Force = \frac{Steady\ State\ Force}{Peak\ Force} \quad (6)$$

Forelimb movement angle analysis

All the videos captured by the high-speed camera underwent 20% slow-motion processing using Adobe PR 2020. Subsequently, we utilized the Deeplabcut 2.2.1 Toolbox for automated trajectory analysis of the videos. Reference points will be marked at the shoulder (S), elbow (E), wrist (W), metacarpophalangeal joints (M), and fingertips (F). These 5 points will be connected sequentially to form three angles representing the elbow, wrist, and metacarpophalangeal joints.

The angles of each joint were calculated in Python using the corresponding CSV files exported by Deeplabcut Toolbox, which were calculated as the difference between the maximum angle among the kinetic positions and the initial angle at the rest position. Results of three repeated induced action was averaged and then used for subsequent statistical analysis.

Furthermore, we used PyCharm Version 2023.1.2 for plotting the kinematic trajectory of the mouse's forelimb. The rest and kinematic position of the forelimbs were marked blue and black, respectively, allowing direct observation of the different evoked actions of the mouse's forelimb.

Statistics analysis

Statistical analyses were performed in GraphPad Prism 9 (GraphPad Software). Data are presented as mean ± s.e.m. Data distributions were tested for normality using the Kolmogorov−Smirnov normality test, and the distribution of the variables in each experimental group was assumed to be normal. So, for comparison of two groups, data were analyzed using unpaired t-test. For comparison of multiple groups, data were analyzed using one-way ANOVA and multiple comparison tests with Dunnett's correct. *$P < 0.05$, **$P < 0.01$, ***$P < 0.001$. $P < 0.05$ was considered statistically significant.

Reporting summary

Further information on research design is available in the Nature Portfolio Reporting Summary linked to this article.

Data availability

All data supporting the findings of this study are available within the article. The Supplementary Information or the Source Data and extra data are available from the corresponding author upon request. Source data are provided with this paper.

References

1. Thayabaranathan, T. et al. Global stroke statistics 2022. *Int. J. Stroke* **17**, 946–956 (2022).

2. Park, T.-Y., Jeon, J., Cha, Y. & Kim, K.-S. Past, present, and future of cell replacement therapy for parkinson's disease: a novel emphasis on host immune responses. *Cell Res.* https://doi.org/10.1038/s41422-024-00971-y (2024).

3. Woo, M. S., Engler, J. B. & Friese, M. A. The neuropathobiology of multiple sclerosis. *Nat. Rev. Neurosci.* https://doi.org/10.1038/s41583-024-00823-z (2024).

4. Kim, R. B., Bounajem, M., Hamrick, F. & Mahan, M. A. Optimal donor nerve to restore elbow flexion after traumatic brachial plexus injury: a systematic review and meta-analysis. *Neurosurgery* **90**, 39–50 (2022).

5. Pengked, K., Laohaprasitiporn, P., Monteerarat, Y., Limthongthang, R. & Vathana, T. Effect of shorter nerve graft and selective motor branch of recipient nerve on nerve transfer surgery for elbow flexion in patients with brachial plexus injury. *J. Neurosurg.* 1–7 https://doi.org/10.3171/2023.1.JNS222836 (2023).

6. Nagano, A., Yamamoto, S. & Mikami, Y. Intercostal nerve transfer to restore upper extremity functions after brachial plexus injury. *Ann. Acad. Med. Singap.* **24**, 42–45 (1995).

7. Zheng, M.-X. et al. Trial of contralateral seventh cervical nerve transfer for spastic arm paralysis. *N. Engl. J. Med.* **378**, 22–34 (2018).

8. Feng, J., Gu, Y. & Xu, W. Hand surgery in a new "hand-brain" era: change the hand, rebuild the brain. *Sci. Bull.* **67**, 1932–1934 (2022).

9. Feng, J. et al. Reconstruction of paralyzed arm function in patients with hemiplegia through contralateral seventh cervical nerve cross transfer: a multicenter study and real-world practice guidance. *EClinicalMedicine* **43**, 101258 (2022).

10. van Zyl, N., Hill, B., Cooper, C., Hahn, J. & Galea, M. P. Expanding traditional tendon-based techniques with nerve transfers for the restoration of upper limb function in tetraplegia: a prospective case series. *Lancet* **394**, 565–575 (2019).

11. Zhao, X. et al. Selective neurotization of the median nerve in the arm to treat brachial plexus palsy. An anatomic study and case report. *J. Bone Jt. Surg. Am.* **86**, 736–742 (2004).

12. Yang, J., Chen, L., Gu, Y., Chen, D. & Wang, T. Selective neurotization of the radial nerve in the axilla using a full-length phrenic nerve to treat complete brachial plexus palsy: an anatomic study and case report. *Neurosurgery* **68**, 1648–1653 (2011).

13. Carnicer-Lombarte, A. et al. Ultraconformable cuff implants for long-term bidirectional interfacing of peripheral nerves at sub-nerve resolutions. *Nat. Commun.* **15**, 7523 (2024).

14. Hempel, B. et al. PPARα and PPARγ are expressed in midbrain dopamine neurons and modulate dopamine- and cannabinoid-mediated behavior in mice. *Mol. Psychiatry* https://doi.org/10.1038/s41380-023-02182-0 (2023).

15. Roe, A. W. BMI 2.0: toward a technological interface with brainwide networks. *Neuron* **111**, 1687–1688 (2023).

16. Welsch, L. et al. Mu opioid receptor-expressing neurons in the dorsal raphe nucleus are involved in reward processing and affective behaviors. *Biol. Psychiatry* S0006-3223(23)01328–8 https://doi.org/10.1016/j.biopsych.2023.05.019 (2023).

17. Wood, E. H. et al. Cellular and subcellular optogenetic approaches towards neuroprotection and vision restoration. *Prog. Retin. Eye Res.* 101153 https://doi.org/10.1016/j.preteyeres.2022.101153 (2022).

18. Bloch, E., Luo, Y. & da Cruz, L. Advances in retinal prosthesis systems. *Ther. Adv. Ophthalmol.* **11**, 2515841418817501 (2019).

19. Gao, Z. et al. Crossing nerve transfer drives sensory input–dependent plasticity for motor recovery after brain injury. *Sci. Adv.* **8**, eabn5899 (2022).

20. Scheib, J. & Höke, A. Advances in peripheral nerve regeneration. *Nat. Rev. Neurol.* **9**, 668–676 (2013).

21. Li, J. et al. The Hua-Shan rehabilitation program after contralateral seventh cervical nerve transfer for spastic arm paralysis. *Disabil. Rehabil.* **44**, 404–411 (2022).

22. Zheng, H. et al. A shape-memory and spiral light-emitting device for precise multisite stimulation of nerve bundles. *Nat. Commun.* **10**, 2790 (2019).

23. Wang, G.-B. et al. Contralateral C7 to C7 nerve root transfer in reconstruction for treatment of total brachial plexus palsy: anatomical basis and preliminary clinical results. *J. Neurosurg. Spine* **29**, 491–499 (2018).

24. Zhang, Y. et al. Battery-free, lightweight, injectable microsystem for in vivo wireless pharmacology and optogenetics. *Proc. Natl. Acad. Sci. USA* **116**, 21427–21437 (2019).

25. Won, S. M., Cai, L., Gutruf, P. & Rogers, J. A. Wireless and battery-free technologies for neuroengineering. *Nat. Biomed. Eng.* **7**, 405–423 (2021).

26. Zhang, Y. et al. Battery-free, fully implantable optofluidic cuff system for wireless optogenetic and pharmacological neuromodulation of peripheral nerves. *Sci. Adv.* **5**, eaaw5296 (2019).

27. Sethi, J., Glowacki, E., Reid, M. S., Larsson, P. A. & Wågberg, L. Ultra-thin parylene-aluminium hybrid coatings on nanocellulose films to resist water sensitivity. *Carbohydr. Polym.* **323**, 121365 (2024).

28. Zhang, Y. et al. Parylene C as an insulating polymer for implantable neural interfaces: acute electrochemical impedance behaviors in saline and pig brain in vitro. *Polymers* **14**, 3033 (2022).

29. Shin, G. Studies of parylene/silicone-coated soft bio-implantable optoelectronic device. *Coatings* **10**, 404 (2020).

30. Song, K.-I. et al. Compact optical nerve cuff electrode for simultaneous neural activity monitoring and optogenetic stimulation of peripheral nerves. *Sci. Rep.* **8**, 15630 (2018).

31. Klapoetke, N. C. et al. Independent optical excitation of distinct neural populations. *Nat. Methods* **11**, 338–346 (2014).

32. Timotius, I. K. et al. CatWalk XT gait parameters: a review of reported parameters in pre-clinical studies of multiple central nervous system and peripheral nervous system disease models. *Front. Behav. Neurosci.* **17**, 1147784 (2023).

33. Bryson, J. B. et al. Optical control of muscle function by transplantation of stem cell–derived motor neurons in mice. *Science* **344**, 94–97 (2014).

34. Herrera-Arcos, G. et al. Closed-loop optogenetic neuromodulation enables high-fidelity fatigue-resistant muscle control. *Sci. Robot.* **9**, eadi8995 (2024).

35. Liske, H. et al. Optical inhibition of motor nerve and muscle activity in vivo. *Muscle Nerve* **47**, 916–921 (2013).

36. Towne, C., Montgomery, K. L., Iyer, S. M., Deisseroth, K. & Delp, S. L. Optogenetic control of targeted peripheral axons in freely moving animals. *PLoS ONE* **8**, e72691 (2013).

37. Park, S. I. et al. Soft, stretchable, fully implantable miniaturized optoelectronic systems for wireless optogenetics. *Nat. Biotechnol.* **33**, 1280–1286 (2015).

38. Koo, J. Wireless bioresorbable electronic system enables sustained nonpharmacological neuroregenerative therapy. *Nat. Med.* **24**, 1830–1836 (2018).

39. Zhang, Y. et al. Self-powered, light-controlled, bioresorbable platforms for programmed drug delivery. *Proc. Natl. Acad. Sci. USA* **120**, e2217734120 (2023).

40. Mickle, A. D. et al. A wireless closed-loop system for optogenetic peripheral neuromodulation. *Nature* **565**, 361–365 (2019).

41. Kathe, C. et al. Wireless closed-loop optogenetics across the entire dorsoventral spinal cord in mice. *Nat. Biotechnol.* **40**, 198–208 (2022).

42. Srinivasan, S. S., Maimon, B. E., Diaz, M., Song, H. & Herr, H. M. Closed-loop functional optogenetic stimulation. *Nat. Commun.* **9**, 5303 (2018).

43. Kumari, L. S. & Kouzani, A. Z. Electrophysiology-based closed loop optogenetic brain stimulation devices: recent developments and future prospects. In *Proc. IEEE Reviews in Biomedical Engineering* (IEEE, 2023).

44. Chen, S. et al. Near-infrared deep brain stimulation via upconversion nanoparticle-mediated optogenetics. *Science* **359**, 679–684 (2018).

45. Jia, Y. et al. Wireless opto-electro neural interface for experiments with small freely behaving animals. *J. Neural Eng.* **15**, 046032 (2018).

46. Yang, L. & Martin, J. H. Effects of motor cortex neuromodulation on the specificity of corticospinal tract spinal axon outgrowth and targeting in rats. *Brain Stimul.* **16**, 759–771 (2023).

47. Karatum, O. et al. Optical neuromodulation at all scales: from nanomaterials to wireless optoelectronics and integrated systems. *Chem. Soc. Rev.* **52**, 3326–3352 (2023).

48. Parameswaran, R. et al. Photoelectrochemical modulation of neuronal activity with free-standing coaxial silicon nanowires. *Nat. Nanotechnol.* **13**, 260–266 (2018).

49. Ecanow, A., Berglund, K., Carrasco, D., Isaacson, R. & English, A. Enhancing motor and sensory axon regeneration after peripheral nerve injury using bioluminescent optogenetics. *IJMS* **23**, 16084 (2022).

50. Ji, Z.-G. & Wang, H. ChR2 transgenic animals in peripheral sensory system: sensing light as various sensations. *Life Sci.* **150**, 95–102 (2016).

51. Ouyang, W. et al. A wireless and battery-less implant for multimodal closed-loop neuromodulation in small animals. *Nat. Biomed. Eng.* https://doi.org/10.1038/s41551-023-01029-x (2023).

52. Ausra, J. et al. Wireless, battery-free, subdermally implantable platforms for transcranial and long-range optogenetics in freely moving animals. *Proc. Natl. Acad. Sci. USA* **118**, e2025775118 (2021).

53. Woods, J. E. et al. Miniature battery-free epidural cortical stimulators. *Sci. Adv.* **10**, eadn0858 (2024).

54. Kim, C. Y. et al. Soft subdermal implant capable of wireless battery charging and programmable controls for applications in optogenetics. *Nat. Commun.* **12**, 535 (2021).

55. Lee, J. et al. Neural recording and stimulation using wireless networks of microimplants. *Nat. Electron* **4**, 604–614 (2021).

56. Ausra, J. et al. Wireless battery free fully implantable multimodal recording and neuromodulation tools for songbirds. *Nat. Commun.* **12**, 1968 (2021).

57. Yang, Y. et al. Wireless multilateral devices for optogenetic studies of individual and social behaviors. *Nat. Neurosci.* **24**, 1035–1045 (2021).

58. Lee, G. et al. A bioresorbable peripheral nerve stimulator for electronic pain block. *Sci. Adv.* **8**, eabp9169 (2022).

59. Guo, H. et al. Advanced materials in wireless, implantable electrical stimulators that offer rapid rates of bioresorption for peripheral axon regeneration. *Adv. Funct. Mater.* **31**, 2102724 (2021).

60. Lee, Y. et al. A low-power stretchable neuromorphic nerve with proprioceptive feedback. *Nat. Biomed. Eng.* https://doi.org/10.1038/s41551-022-00918-x (2022).

61. Burton, A. et al. Fully implanted battery-free high power platform for chronic spinal and muscular functional electrical stimulation. *Nat. Commun.* **14**, 7887 (2023).

62. Kutzner, C. E. et al. Optogenetic induction of mechanical muscle stress identifies myosin regulatory ubiquitin ligase NHL-1 in C. elegans. *Nat. Commun.* **15**, 6879 (2024).

63. Ganji, E., Chan, C. S., Ward, C. W. & Killian, M. L. Optogenetic activation of muscle contraction in vivo. *Connect. Tissue Res.* **62**, 15–23 (2021).

64. Ganji, E. et al. Optogenetic-induced muscle loading leads to mechanical adaptation of the Achilles tendon enthesis in mice. *Sci. Adv.* **9**, eadf4683 (2023).

65. Raman, R. et al. Optogenetic skeletal muscle-powered adaptive biological machines. *Proc. Natl. Acad. Sci. USA* **113**, 3497–3502 (2016).

66. Barra, B. et al. Epidural electrical stimulation of the cervical dorsal roots restores voluntary upper limb control in paralyzed monkeys. *Nat. Neurosci.* **25**, 924–934 (2022).

67. Adcock, K. S. et al. Radial nerve injury causes long-lasting forelimb sensory impairment and motor dysfunction in rats. *Pain. Rep.* **6**, e957 (2021).

68. Ljungquist, K. L., Martineau, P. & Allan, C. Radial nerve injuries. *J. Hand Surg. Am.* **40**, 166–172 (2015).

69. Zhao, X. et al. Selective neurotization of the median nerve in the arm to treat brachial plexus palsy. Surgical technique. *J. Bone Jt. Surg. Am.* **87**, 122–135 (2005).

70. Planitzer, U. et al. Median nerve fascicular anatomy as a basis for distal neural prostheses. *Ann. Anat.* **196**, 144–149 (2014).

71. Chambers, S. B. et al. Interfascicular anatomy of the motor branch of the ulnar nerve: a cadaveric study. *J. Hand Surg. Am.* **48**, 309.e1–309.e6 (2023).

72. Pautler, B., Marchese, C., Swancutt, M. & Beutel, B. G. Anatomical characterization and topographic mapping of the distal ulnar nerve and its peripheral branches: a cadaveric analysis. *Hand* 1558944 7241306151 https://doi.org/10.1177/15589447241306151 (2024).

73. Rowald, A. et al. Activity-dependent spinal cord neuromodulation rapidly restores trunk and leg motor functions after complete paralysis. *Nat. Med.* **28**, 260–271 (2022).

74. Kathe, C. et al. The neurons that restore walking after paralysis. *Nature* **611**, 540–547 (2022).

75. Ward, P. J., Clanton, S. L. & English, A. W. Optogenetically enhanced axon regeneration: motor versus sensory neuron-specific stimulation. *Eur. J. Neurosci.* **47**, 294–304 (2018).

76. Liu, X. et al. Fatigue-resistant hydrogel optical fibers enable peripheral nerve optogenetics during locomotion. *Nat. Methods* **20**, 1802–1809 (2023).

77. Yuk, H., Lu, B. & Zhao, X. Hydrogel bioelectronics. *Chem. Soc. Rev.* **48**, 1642–1667 (2019).

78. Ryu, H., Seo, M.-H. & Rogers, J. A. Bioresorbable metals for biomedical applications: from mechanical components to electronic devices. *Adv. Health. Mater.* **10**, e2002236 (2021).

79. Lee, D.-M. et al. An on-demand bioresorbable neurostimulator. *Nat. Commun.* **14**, 7315 (2023).

80. Thompson, A. C., Wade, S. A., Brown, W. G. A. & Stoddart, P. R. Modeling of light absorption in tissue during infrared neural stimulation. *J. Biomed. Opt.* **17**, 0750021 (2012).

81. Goldfain, A. M., Lemaillet, P., Allen, D. W., Briggman, K. A. & Hwang, J. Polydimethylsiloxane tissue-mimicking phantoms with tunable optical properties. *J. Biomed. Opt.* **27**, (2021).

82. Durian, D. J. The diffusion coefficient depends on absorption. *Opt. Lett.* **23**, 1502 (1998).

83. Markos, C., Vlachos, K. & Kakarantzas, G. Guiding and thermal properties of a hybrid polymer-infused photonic crystal fiber. *Opt. Mater. Express* **2**, 929 (2012).

Acknowledgements

Author contributions

M.Z. and F.Y. wrote the original draft; F.Y. and C.W. designed the electronics, firmware and software and conducted finite-element analysis; M.Z. and F.Y. designed the optogenetic cuff; F.Y., C.W., and Y.X. fabricated the device; F.Y., K.L., Y.X., H.Z., and C.W. conducted the device experiments; M.Z., C.C., C.X., T.J., F.W., and S.J. conducted the animal-model experiments; M.Z., B.Y., and H.Z. analyzed the data and printed

the figures; F.W., S.J., and J.Z. reviewed the manuscript. All authors read and approved the final manuscript.

Competing interests

The authors declare no competing interests.

Additional information